Production of Protons and Light Nuclei in Au+Au Collisions at $\sqrt{s_{\rm NN}} = 3\,{\rm GeV}$ with the STAR Detector

The STAR Collaboration

We report the systematic measurement of protons and light nuclei production in Au+Au collisions at $\sqrt{s_{\rm NN}} = 3\,{\rm GeV}$ by the STAR experiment at the Relativistic Heavy Ion Collider (RHIC). The transverse momentum (p_T) spectra of protons (p), deuterons (d), tritons (t), ^{3}He, and ^{4}He are measured from mid-rapidity to target rapidity for different collision centralities. We present the rapidity and centrality dependence of particle yields (dN/dy), average transverse momentum ($\langle p_T \rangle$), yield ratios (d/p, t/p,^{3}He$/p$, ^{4}He$/p$), as well as the coalescence parameters (B_2, B_3). The 4π yields for various particles are determined by utilizing the measured rapidity distributions, dN/dy. Furthermore, we present the energy, centrality and rapidity dependence of the compound yield ratios ($N_p \times N_t/N_d^2$) and compare them with various model calculations. The physics implications of those results on the production mechanism of light nuclei and on QCD phase structure are discussed.

I. INTRODUCTION

Relativistic heavy-ion collisions provide a unique experimental tool to investigate the Quantum Chromodynamics (QCD) phase diagram and the properties of strongly interacting nuclear matter under extreme conditions [1–5]. At vanishing baryon chemical potential ($\mu_B = 0$ MeV), Lattice QCD calculations reveal that the transition between hadronic matter and a Quark-Gluon Plasma (QGP) is a smooth crossover [6]. The QCD-based model predicts that there is a first-order phase transition and a critical point (CP) at high μ_B [7–9]. Mapping the QCD phase structure at high baryon density, namely the first-order phase transition boundary and the location of the CP, is the primary goal of the Beam Energy Scan (BES) program at the Relativistic Heavy-ion Collider (RHIC) [10, 11]. During 2010-2021, RHIC has completed the data taking of the two phases of RHIC BES (BES-I and BES-II) in succession, and the STAR experiment has collected data of Au+Au collisions at $\sqrt{s_{\rm NN}}$ = 7.7 – 200 GeV with collider mode. In addition, the STAR detector was running in Fixed-Target (FXT) mode and took the data of Au+Au collisions at $\sqrt{s_{\rm NN}} = 3$ – 7.7 GeV, which allows us to access the QCD phase diagram with μ_B up to about 750 MeV.

Light nuclei are loosely bound objects with binding energies of a few MeV. In the past half century, their production in heavy-ion collisions at wide energy ranges has been extensively studied both experimentally [12–24] and theoretically [25–38]. Nucleon coalescence and thermal emission are the two most popular mechanisms that are proposed to explain the production of light nuclei in heavy-ion collisions. Based on the coalescence model, it is predicted that the compound yield ratio $N_p \times N_t/N_d^2$ is sensitive to the neutron density fluctuations and can be applied as a sensitive observable to search for the first-order phase transition and/or CP [39, 40]. In RHIC BES-I, the STAR experiment measured the production of deuterons [23] and tritons [24] in Au+Au collisions at $\sqrt{s_{\rm NN}} = 7.7$ – 200 GeV. An enhancement of $N_p \times N_t/N_d^2$ relative to the coalescence baseline was observed in the 0-10% central Au+Au collisions at $\sqrt{s_{\rm NN}} = 19.6$ and 27 GeV with a combined significance of 4.1σ [24]. To determine whether the enhancements are related to a first-order phase transition or CP, dynamical modeling of heavy-ion collisions with a realistic equation of state is needed to compare with the experimental data. In addition, it was observed that the yield ratio $N_p \times N_t/N_d^2$ monotonically decreases with increasing of the charged-particle multiplicity ($dN/d\eta$) and exhibited a scaling behavior [24]. The observed decreasing trend and scaling behavior can be nicely explained by coalescence models while the thermal model predicts an opposite trend. Thus, the systematic measurement of light nuclei production in heavy-ion collisions across a wide energy range serves as a valuable tool not only to probe the QCD phase structure, but also to gain insight into the underlying production mechanism.

In this paper, we present the transverse momentum (p_T) spectra of protons (p), deuterons (d), tritons (t), ^{3}He, and ^{4}He in FXT Au+Au collisions at $\sqrt{s_{\rm NN}} = 3$ GeV. The analysis encompasses four centrality ranges (0-10%, 10-20%, 20-40%, and 40-80%) and spans from mid-rapidity to target rapidity. The proton spectra were obtained by subtracting the contributions from weak decays of hyperons. For light nuclei, no correction for feed-down effects from excited states was applied, and we report their inclusive yields. By fitting the p_T spectra with a blast-wave model, we obtained the centrality and rapidity dependence of dN/dy and $\langle p_T \rangle$ for various particles. Due to broad rapidity coverage, the 4π yields can be obtained by integrating the particle dN/dy from mid-rapidity to target rapidity. We further compare the measured yield and yield ratios of protons and light nuclei with calculations from various transport models, including the Jet AA Microscopic Transportation Model (JAM) [41], Simulating Many Accelerated Strongly-interacting Hadrons (SMASH) [42], Ultra-relativistic Quantum Molecular Dynamics (UrQMD) [43], and Parton Hadron Quantum Molecular Dynamics (PHQMD) [44] models. In these model calculations, except PHQMD, the light nuclei were produced from nucleon coalescence based on the formation probability from the Wigner function [45, 46]. Fi-

nally, we discuss the beam energy dependence of the coalescence parameters (B_2, B_3) and particle yield ratios (d/p, t/p, $N_p \times N_t/N_d^2$).

II. EXPERIMENT AND DATA ANALYSIS

A. Dataset and Event Selection

The STAR Fixed-Target (FXT) program [47, 48] was conducted to achieve lower center-of-mass energies, thus higher baryon density. The gold foil target, whose thickness of 250 μm corresponds to a 1% interaction probability [48, 49], was installed in the vacuum pipe at 200.7 cm to the west of the nominal interaction point and 2 cm down from the central beam-pipe axis of the STAR detector. The experimental data was obtained by

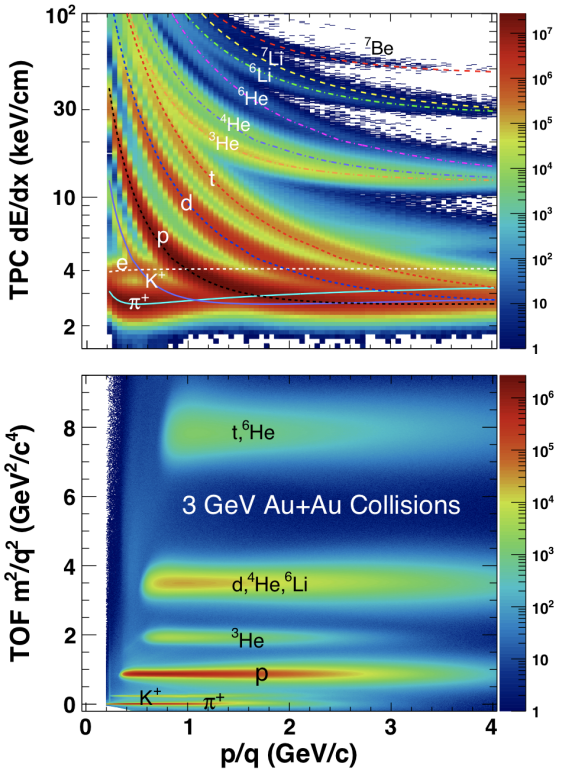

FIG. 1. (top) The $\langle dE/dx \rangle$ of charged tracks versus particle rigidity from Au+Au collisions at $\sqrt{s_{\rm NN}} = 3$ GeV. The lines are Bichsel theoretical curves for the corresponding particles. (bottom) The m^2/q^2 of particle versus rigidity distribution.

bombarding the gold (Au) target with a gold beam of 3.85 GeV/u. The corresponding center-of-mass energy is $\sqrt{s_{\rm NN}} = 3$ GeV. The collision vertex of each event was required to have a z-coordinate (parallel to the beam axis) located within 2 cm of the detector's fixed target position (set $198 \leq {\rm V_Z} \leq 202$ cm for this analysis), and a transverse (x, y) position that lies within a circle of radius 2 cm whose center lies within 2 cm of the beamline (set ${\rm V_x^2} + ({\rm V_y} + 2)^2 < (2{\rm cm})^2$ for this analysis). In total, about 260 million minimum-biased events were retained after applying offline event selection criteria with careful quality assurance. The selection of minimum-biased events was realized by simultaneously detecting multiple signals from the Beam-Beam Counter (BBC) [50] and Time of Flight (TOF) [51] detector systems. Collision centralities were determined by Glauber model fitting of the charged-particle multiplicity measured within the pseudo-rapidity range $-2 < \eta < 0$ (FXTMult). In the analysis, four centrality bins (0-10%, 10-20%, 20-40%, and 40-80%) were used. The FXTMult ranges and the mean values of the number of participating nucleons $\langle N_{\rm Part} \rangle$ for the corresponding centrality bins are shown in Table I.

TABLE I. Centrality definition and the corresponding mean value of $\langle N_{\rm Part} \rangle$ along with the statistical and systematic uncertainties in Au+Au collisions at $\sqrt{s_{\rm NN}} = 3$ GeV.

Centrality	FXTMult	$\langle N_{\rm Part} \rangle$
$0 - 10\%$	$195 - 119$	$310.7 \pm 0.1 \pm 8.3$
$10 - 20\%$	$118 - 86$	$224.2 \pm 0.1 \pm 8.0$
$20 - 40\%$	$85 - 41$	$135.0 \pm 0.1 \pm 5.3$
$40 - 80\%$	$40 - 5$	$39.7 \pm 0.1 \pm 1.9$

B. Track Selection and Particle Identification

In the analysis, particle identification was done with the Time Projection Chamber (TPC) [52] and the Time of Flight (TOF) [51]. To ensure the track quality, it was required that at least 20 of the maximum 45 possible hits (nHitsFit) in the TPC were used to reconstruct the tracks. To avoid counting the reconstructed tracks of individual particles multiple times, more than 52% of the maximum possible fit points were required. In addition, the number of points (nHitsDedx) used to calculate the energy loss (dE/dx) value was also required to be greater than 10. The distance of the closest approach (DCA) from the reconstructed track to the primary vertex was required to be less than 3 cm for protons and 1 cm for light nuclei, in order to suppress contamination from spallation in the beam pipe. In the TOF measurement, an additional filter was implemented to include the local position of the hit in radial (Y-axis) and beam (Z-axis) directions: |btofYLocal| < 1.8 cm and |btofZLocal| < 2.8 cm.

The top panel of Fig. 1 shows the ionization energy loss of charged-particles (dE/dx) measured by the TPC versus particle rigidity (p/q), where q is the particle charge. To identify the specified particles, the variables $n\sigma_p$ and Z were defined as:

$$n\sigma_p = \frac{1}{\sigma_R} \ln \frac{\langle dE/dx \rangle}{\langle dE/dx \rangle^p_{Bichsel}} \quad (1)$$

$$Z = \ln \frac{\langle dE/dx \rangle}{\langle dE/dx \rangle_{Bichsel}} \quad (2)$$

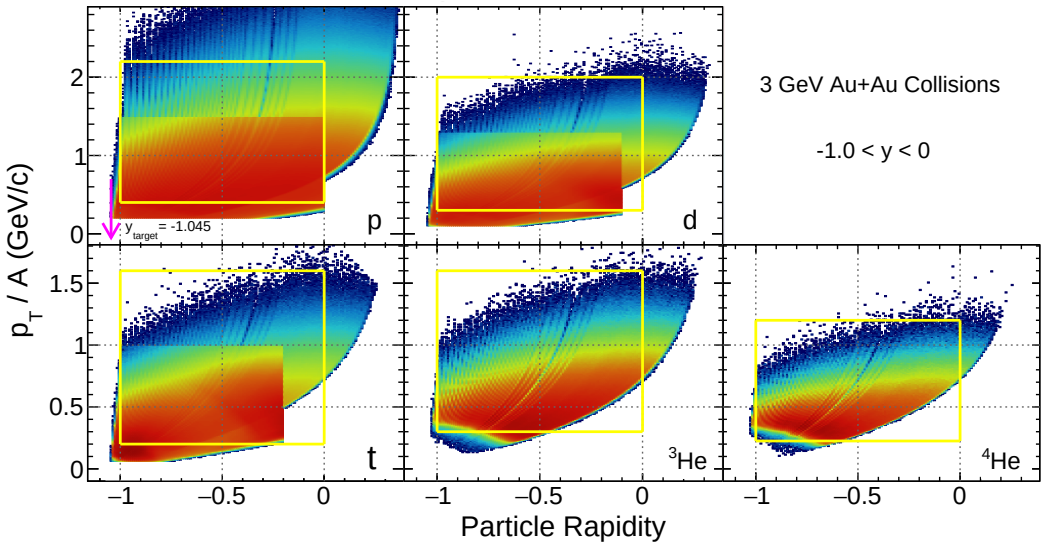

FIG. 2. Atomic mass number normalized transverse momentum (p_T/A) versus rapidity distributions for identified protons, deuterons, tritons, ^{3}He, and ^{4}He. For protons, deuterons, and tritons, the portion identified only by TPC is superimposed. Yellow boxes indicate the region for further analysis.

where the $\langle dE/dx\rangle_{Bichsel}$ is the theoretical value of the energy loss obtained from the Bichsel function [53], which was represented by a dashed line in the figure, and σ_R is the TPC $\ln\langle dE/dx\rangle$ resolution ($\sim 8\%$). At low momentum, the raw signal of protons was obtained by fitting a Gaussian function to the distribution of $n\sigma_p$ [54], and the raw signal of light nuclei was obtained by fitting a Gaussian function to the Z-distribution described in Eq. 2. At high momentum, the raw signal was extracted by using the mass squared (m^2) distributions from the TOF detector, in addition to the $n\sigma_p$ or Z information. The m^2 was calculated as

$$m^2 = p^2\left(\frac{1}{\beta^2} - 1\right) \tag{3}$$

where p is the momentum of the particle, $\beta = L/ct$, and L, c, t are the track path length, speed of light, and time of flight, respectively. Table II shows the rapidity ranges and transverse momentum (p_T) cutoffs for particle identification using TPC and TOF, the rapidity mentioned in this article is the rapidity under the center-of-mass frame.

The bottom panel of Fig. 1 shows the particle m^2 versus particle rigidity (p/q). One can observe that there are very clear bands in the m^2 distribution of different particles. The signal of the particles can be extracted by fitting the m^2 distribution with the Student-t function [23, 55] and an exponential background tail. Consistent with general particle identification, we relied on the dE/dx from TPC for particles in the low p_T region. However, it became evident that using only TPC information was insufficient for accurately identifying deuterons in the $-0.1 < y < 0$ rapidity range and tritons in the $-0.2 < y < 0$ range. Consequently, we incorporated TOF in these specific rapidity ranges even at low p_T. Figure 2 shows the phase space coverage (p_T versus rapidity) for each particle. The rapidity range measured for each particle in this analysis was -1.0 to 0, which is denoted by yellow boxes in Fig. 2.

TABLE II. The p_T range (in GeV/c) of PID by TPC or TPC+TOF for different particles.

Particle	TPC	TPC+TOF
proton	$p_T \leq 1.5$	$p_T > 1.5$
deuteron($-0.1 < y < 0$)	—	$p_T > 0.6$
deuteron($-1.0 < y < -0.1$)	$p_T \leq 2.6$	$p_T > 2.6$
triton($-0.2 < y < 0$)	—	$p_T > 0.6$
triton($-1.0 < y < -0.2$)	$p_T \leq 3.0$	$p_T > 3.0$
^{3}He	—	$p_T \geq 0.9$
^{4}He	—	$p_T \geq 0.9$

C. Efficiency Correction and Energy Loss Correction

In order to obtain final particle spectra in each rapidity interval, efficiency correction and energy loss correction needed to be done. The TPC tracking efficiency and acceptance were determined by the so-called embedding technique. The technique is to embed sampled Monte Carlo (MC) tracks, within a given kinematic range, simulated using a GEANT model [56, 57] of the STAR detector and detector response simulators, into real events at the raw data level to determine the quality and quantity of the reconstructed embedded tracks. The acceptance and reconstruction efficiency is finally given by the ratio of reconstructed tracks to embedded MC tracks, as

TABLE III. Weak decay feed-down fraction of protons (%) at different centralities in Au+Au collisions at $\sqrt{s_{\rm NN}} = 3\,$GeV. The uncertainties represent statistical and systematic uncertainties, respectively.

Rapidity	0-10%	10-20%	20-40%	40-80%
-0.1 < y < 0	1.838 ± 0.017 ± 0.214	1.642 ± 0.013 ± 0.184	1.500 ± 0.006 ± 0.173	1.046 ± 0.002 ± 0.140
-0.2 < y < -0.1	1.984 ± 0.017 ± 0.198	1.774 ± 0.012 ± 0.182	1.511 ± 0.006 ± 0.167	1.016 ± 0.002 ± 0.103
-0.3 < y < -0.2	2.029 ± 0.015 ± 0.188	1.809 ± 0.011 ± 0.162	1.481 ± 0.005 ± 0.148	2.901 ± 0.004 ± 0.333
-0.4 < y < -0.3	1.895 ± 0.014 ± 0.197	1.637 ± 0.010 ± 0.147	1.490 ± 0.005 ± 0.155	0.969 ± 0.001 ± 0.084
-0.5 < y < -0.4	1.813 ± 0.013 ± 0.168	1.616 ± 0.010 ± 0.154	1.288 ± 0.005 ± 0.119	0.816 ± 0.001 ± 0.094
-0.6 < y < -0.5	1.685 ± 0.012 ± 0.155	1.456 ± 0.009 ± 0.127	1.182 ± 0.004 ± 0.119	0.718 ± 0.001 ± 0.093
-0.7 < y < -0.6	1.490 ± 0.010 ± 0.140	1.355 ± 0.009 ± 0.112	1.034 ± 0.004 ± 0.090	0.722 ± 0.001 ± 0.086
-0.8 < y < -0.7	1.299 ± 0.008 ± 0.117	1.121 ± 0.007 ± 0.088	0.854 ± 0.003 ± 0.080	0.569 ± 0.001 ± 0.103
-0.9 < y < -0.8	1.096 ± 0.007 ± 0.086	0.866 ± 0.005 ± 0.073	0.699 ± 0.003 ± 0.079	0.293 ± 0.001 ± 0.059
-1.0 < y < -0.9	1.141 ± 0.006 ± 0.102	0.883 ± 0.005 ± 0.100	0.687 ± 0.003 ± 0.065	0.329 ± 0.001 ± 0.072

shown by Eq. 4:

$$\varepsilon_{\rm TPC} = \frac{N_{\rm rec.}(\text{Track quality cuts})}{N_{\rm emb.}} \tag{4}$$

where $N_{\rm rec.}$ and $N_{\rm emb.}$ are the number of reconstructed MC tracks satisfying the track quality cuts and the number of embedded MC tracks, respectively. The TOF matching efficiency is defined as the ratio between the number of tracks matched with TOF and the number of tracks identified by TPC.

Low-momentum particles experience a substantial energy loss while traversing the detector material. Thus, it is necessary to correct the energy loss of these particles, especially the heavier ones. The energy loss can be corrected with the embedding data by comparing the p_T difference between the reconstructed and embedded MC tracks. The p_T-dependent correction factor was parametrized with Eq. 5.

$$p_T^{rec.} - p_T^{MC} = p_0 + p_1 \left(1 + \frac{p_2}{(p_T^{rec.})^2}\right)^{p_3} \tag{5}$$

where p_0, p_1, p_2, and p_3 are the fit parameters. For each particle, a set of fit parameters was obtained to estimate the p_T-dependent energy loss effect. These parameters were utilized to correct the final particle p_T when accounting for these efficiencies.

A potential source of background contamination in the spectra and yield analysis are knockout-particles produced through interactions of high-energy particles with detectors materials or the beam pipe. We completed a full GEANT simulation of the STAR detector with 1 million UrQMD Au+Au events at $\sqrt{s_{\rm NN}} = 3\,$GeV and found that knockout-particles constitute less that 2% of the background contamination in the measured acceptance region. Therefore, no knockout correction was applied.

D. Weak decay Feed-down Correction for Protons

In heavy-ion collisions, weak decays of strange baryons, such as Λ and Ξ and their anti-particles, will contribute to the final yields of the (anti-)protons [58–60]. To obtain the primordial yields of (anti-)protons, it is necessary to subtract the contributions from weak decay. As reported in Ref. [24], the STAR experiment has published the energy dependence of the weak decay fractions for (anti-)protons in Au+Au collisions at $\sqrt{s_{\rm NN}} = 7.7 - 200\,$GeV. Similarly to the previous analysis, for 3 GeV the measured p_T spectra of Λ and Ξ^- [61] were used as inputs for the embedding to simulate the decay kinematics of hyperons and p_T spectra of the daughter protons. The main decay channels and branching ratios (BR) are shown below [62]:

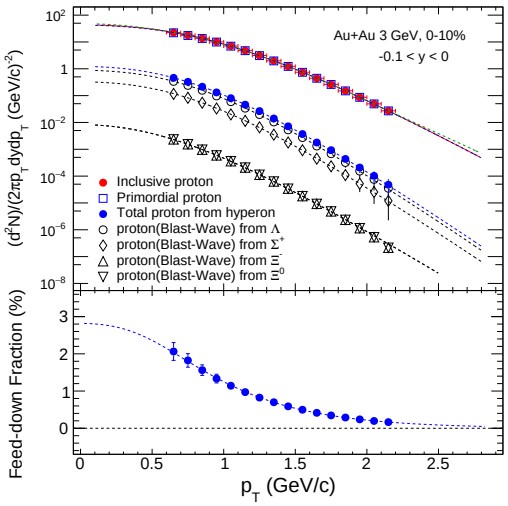

FIG. 3. The p_T dependence of the inclusive, primordial, and weak decay feed-down fraction of proton yields in Au+Au collisions at $\sqrt{s_{\rm NN}} = 3\,$GeV. The dashed/solied line corresponding to the marker color is the fitting result of the blast-wave model of the corresponding particle.

$$\Lambda \longrightarrow p + \pi^-, \text{BR} = 63.9\%$$

$$\Sigma^+ \longrightarrow p + \pi^0, \text{BR} = 51.57\%$$

$$\Xi^- \longrightarrow \Lambda + \pi^-, \text{BR} = 99.887\%$$

$$\Xi^0 \longrightarrow \Lambda + \pi^0, \text{BR} = 99.524\%.$$

The p_T spectra of Σ^+ was obtained by multiplying the Λ spectra by a factor of 0.224 ($\Sigma^+/\Lambda = 0.224$ was estimated from the thermal model). Based on the ART [63] calculation, we assumed the spectra of Ξ^0 and Ξ^- are the same and took 30% of the Ξ^0 yield into the estimate of uncertainty.

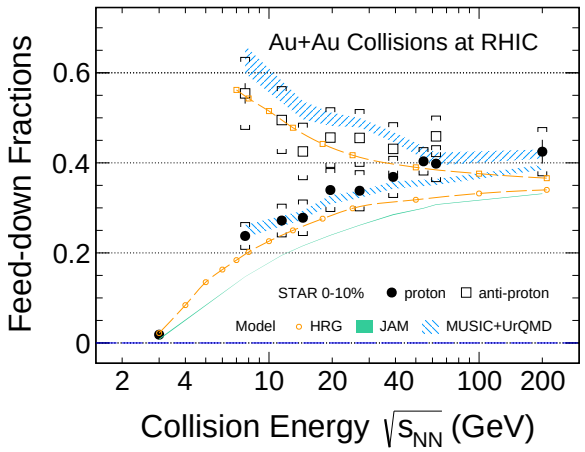

FIG. 4. Energy dependence of the weak decay feed-down fraction of protons (filled circle), and anti-protons (open squares) in 0-10% Au+Au collisions at RHIC, determined using a data-driven approach. The calculations from HRG (orange marker), JAM (dark-green band), and MUSIC+UrQMD (dashed-blue area) models are plotted for comparison.

As shown in Fig. 3, the top panel includes the p_T spectra of the inclusive protons, the protons from the weak-decay of strange baryons and the primordial protons at mid-rapidity in 0-10% Au+Au collisions at $\sqrt{s_{\rm NN}}$ = 3 GeV. The bottom panel shows the p_T dependence of the fraction from the feed-down contribution. Finally, the obtained weak decay feed-down fractions of protons for each centrality and rapidity window were listed in Table III. The maximum contribution for the yield of protons from weak decay feed-down is about 2%. The statistical uncertainties of the weak decay fractions were obtained by adding the statistical uncertainties from different particle spectra in quadrature. The systematic uncertainty is the orthogonal addition of two parts, the first part is the systematic uncertainty of the primordial protons (5-7%), and the second part is the difference between the double p_T^2 exponential function and blast-wave model (6-9%).

Figure 4 shows the energy dependence of the weak decay feed-down fraction for protons and anti-protons at mid-rapidity in 0-10% central Au+Au collisions. The filled circles and open squares are the results of protons and anti-protons, respectively. While the weak decayed proton fractions decrease as collision energy decreases, the fractions of anti-protons show the opposite trend. At high energies, the two fractions approach each other and reach saturation around ∼40%. The weak decay fraction of (anti-)protons calculated from the hadron resonance gas (HRG) [64] and MUSIC+UrQMD [38] models show good agreement with the measured data while the JAM model underestimates the feed-down fractions with respect to our results.

E. Systematic Uncertainty

There are two dominant sources of systematic uncertainties for the p_T spectra. The first one comes from the variation of the track quality cuts, such as nHitsFit, nHitsDedx, and DCA. The other one is from the uncertainty of the tracking efficiency obtained by the embedding simulation and 5% was quoted for all particles. The details of the systematic uncertainty for all particles are shown in Table IV.

TABLE IV. Systematic uncertainty of the particle p_T spectra at all rapidity and centrality ranges.

Sources	p	d	t	^{3}He	^{4}He
nHitsFit	3−5%	2−4%	3−5%	2−3%	1−5%
nHitsDedx	1−2%	1−2%	1−2%	1−2%	1−4%
DCA	3−6%	1−4%	3−5%	1−3%	1−5%
Cuts (total)	3−7%	2−5%	3−6%	2−4%	2−6%
Tracking eff.	5%	5%	5%	5%	5%

The p_T integral yield (dN/dy) for various particles was obtained by adding the yields in the measured p_T region and the unmeasured p_T range, which was extrapolated from the blast-wave function [65]. The main source of systematic uncertainty for dN/dy originated from the extrapolation of the unmeasured yield at low p_T region. This uncertainty was estimated by using double p_T^2 exponential function to fit the p_T spectra and comparing the corresponding extrapolated yields to the default ones obtained from the blast-wave model. The systematic uncertainties from the extrapolation at different centralities are about 3-6% for protons and increases for light nuclei with a maximum contribution to 18% for ^{4}He. The final systematic uncertainties were calculated by using quadrature summation of the uncertainties from extrapolation and tracking efficiency. The total uncertainties were about 6-8% for protons, 6-12% for deuteron, 6-11% for triton, 7-11% for ^{3}He, and 6-20% for ^{4}He, respectively.

For the systematic uncertainties of compound yield ratios, the default yield ratios were obtained by fitting the spectra with the blast-wave model. Different functions, such as the double p_T exponential function, Boltzmann function, Levy function, and m_T exponential function were also applied to calculate the yield ratio. The differences between those results and the default value were the main source of systematic uncertainty. The total systematic uncertainty for the ratio ($N_p \times N_t/N_d^2$) was about 2-15% for different rapidity and centrality bins. The systematic uncertainty increased to 25% when we considered ^{3}He, and ^{4}He in the yield ratio.

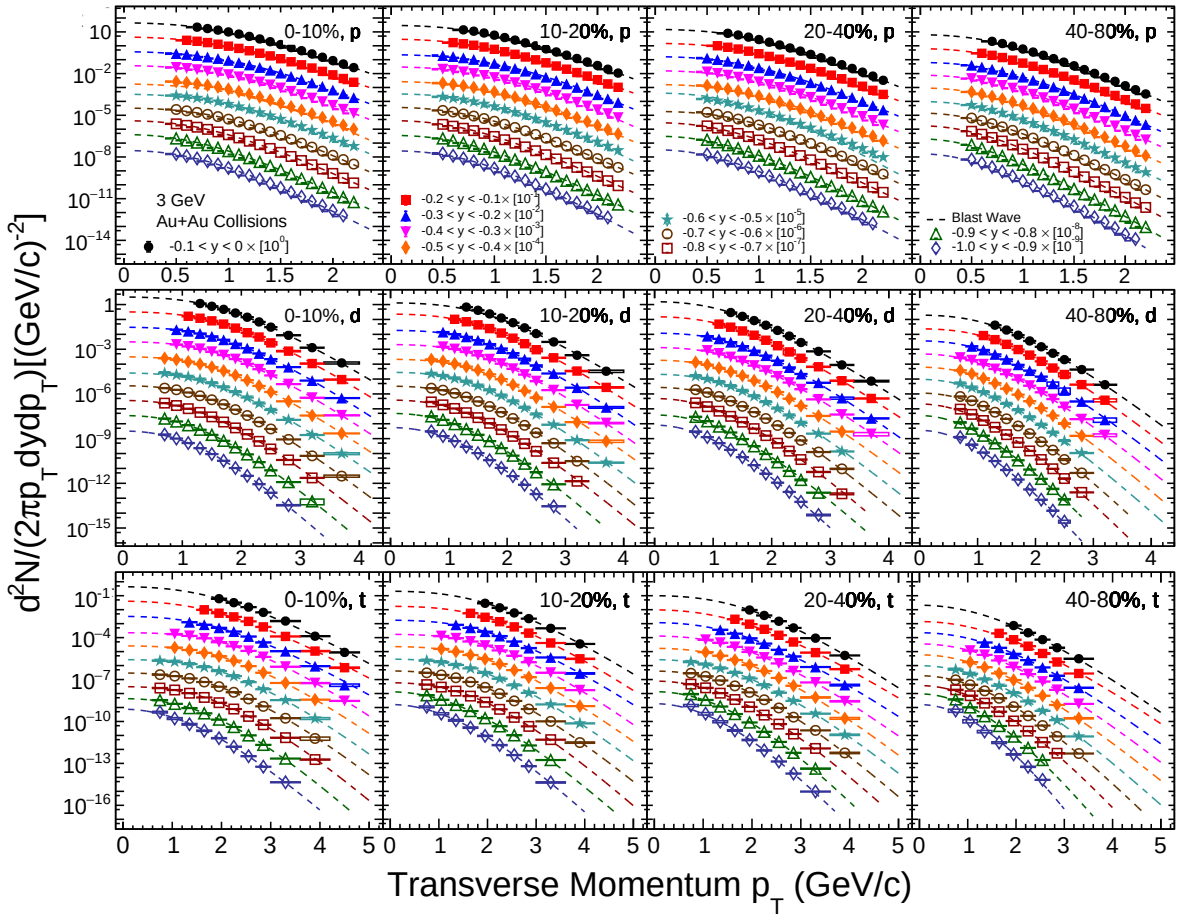

FIG. 5. Transverse momentum spectra (p_T) of protons (top), deuterons (middle), and tritons (bottom) from different rapidity ranges and centrality bins in Au+Au collisions at $\sqrt{s_{\rm NN}} = 3\,{\rm GeV}$. For illustration purposes, those spectra are scaled by a factor from 1 at mid-rapidity to 10^{-9} at target rapidity. Systematic uncertainties are represented by boxes. The dotted lines are blast-wave model fits.

III. RESULTS AND DISCUSSIONS

A. Transverse Momentum Spectra

Figures 5 and 6 show the transverse momentum spectra (p_T) for primordial protons, deuterons, tritons, ^{3}He and ^{4}He in 0-10%, 10-20%, 20-40%, and 40-80% central Au+Au collisions at $\sqrt{s_{\rm NN}} = 3\,{\rm GeV}$. The results are shown in various rapidity windows with a bin width of 0.1. For illustration purposes, the data points were scaled by a factor from 1 at mid-rapidity to 10^{-9} at target rapidity. The dotted lines represent the blast-wave model fit, which can be expressed by Eq. 6:

$$\frac{1}{2\pi p_T}\frac{d^2N}{dp_T dy} \propto \int_0^R r dr m_T I_0\left(\frac{p_T \sinh\rho(r)}{T_{kin}}\right) \times K_1\left(\frac{m_T \cosh\rho(r)}{T_{kin}}\right) \quad (6)$$

where m_T is the transverse mass of particle, I_0 and K_1 are the modified Bessel functions, T_{kin} is the kinetic freeze-out temperature, and $\rho(r) = \tanh^{-1}\beta_T$ is the velocity profile, respectively. The transverse radial flow velocity β_T in the region $0 \le r \le R$ can be expressed as $\beta_T = \beta_S(r/R)^n$, where β_S is the surface velocity, r/R is relative radial extent of the thermal source, and the exponent n reflects the form of the flow velocity profile (fixed $n = 1$ in this analysis).

B. Averaged Transverse Momentum ($\langle p_T\rangle$)

The averaged transverse momentum $\langle p_T\rangle$ was calculated from the measured p_T range and extrapolated to the unmeasured region with individual blast-wave model fits. The rapidity dependence of $\langle p_T\rangle$ for $p, d, t, ^3$He, and ^{4}He in 0-10%, 10-20%, 20-40%, and 40-80% Au+Au collisions at $\sqrt{s_{\rm NN}} = 3\,{\rm GeV}$ are shown in Fig. 7. The $\langle p_T\rangle$ of each particle shows a trend of monotonically decreasing from mid-rapidity to target rapidity and from central to peripheral collisions.

For the $\langle p_T\rangle$ of particles, the systematic uncertainties were estimated in the same way as for dN/dy and the

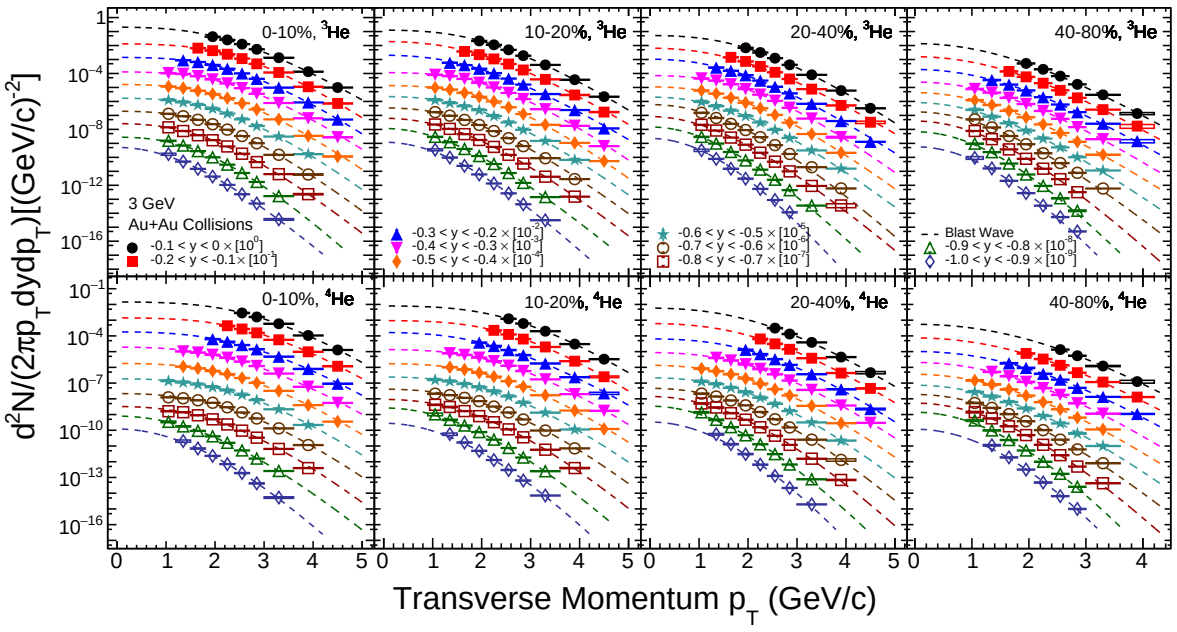

FIG. 6. Similar to Fig. 5, ^{3}He (top) and ^{4}He (bottom) transverse momentum spectra (p_T) from different rapidity ranges and centrality bins.

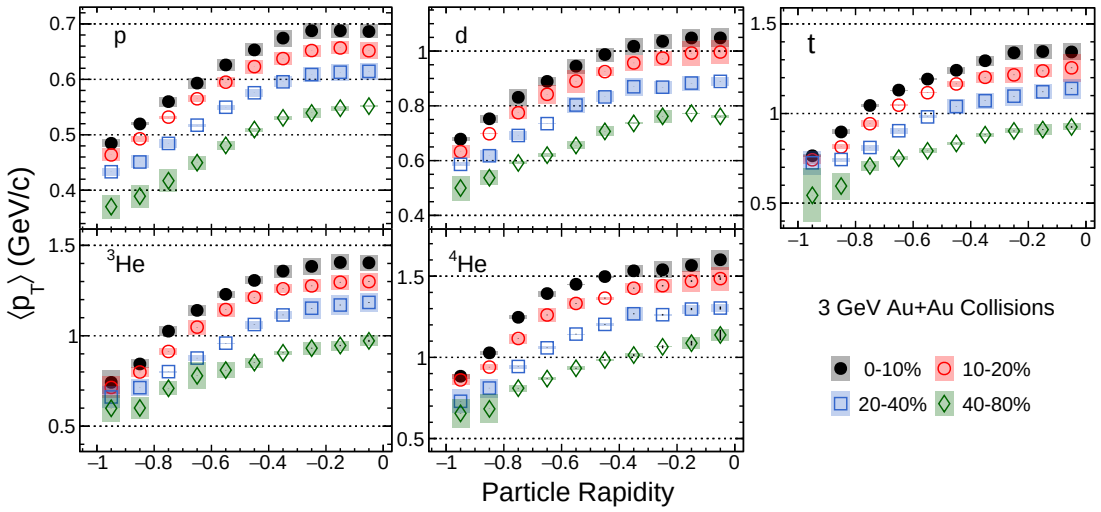

FIG. 7. Collision centrality and particle rapidity dependence of averaged transverse momentum $\langle p_T \rangle$ of protons and light nuclei from Au+Au collisions at $\sqrt{s_{\rm NN}} = 3$ GeV. The boxes indicate systematic uncertainties.

total systematic uncertainties on $\langle p_T \rangle$ are 1-3% for protons, 3-9% for deuterons, 5-13% for tritons, 3-12% for ^{3}He, and 3-12% for ^{4}He.

C. dN/dy and 4π Yields of Particles

Figure 8 shows the rapidity dependence of the p_T integrated yield (dN/dy) for primordial protons and light nuclei in 0-10%, 10-20%, 20-40%, and 40-80% central Au+Au collisions at $\sqrt{s_{\rm NN}} = 3$ GeV. In each panel, different markers represent the distributions for different particles. Due to the interplay between baryon stopping and spectators' contribution, the dN/dy of protons and deuterons decrease from mid-rapidity to target rapidity in the 0-10% most central collisions, while in peripheral collisions, the values of dN/dy are peaked near the target rapidity. For tritons, ^{3}He, and ^{4}He, the peak structures at target rapidity are increasingly prominent as we move from central to peripheral collisions, due primarily to the fragmentation of the spectators [66]. The measured dN/dy for various particles were listed in Table V and Table VI. At the same time, considering the significant contribution of the extrapolated p_T range to the

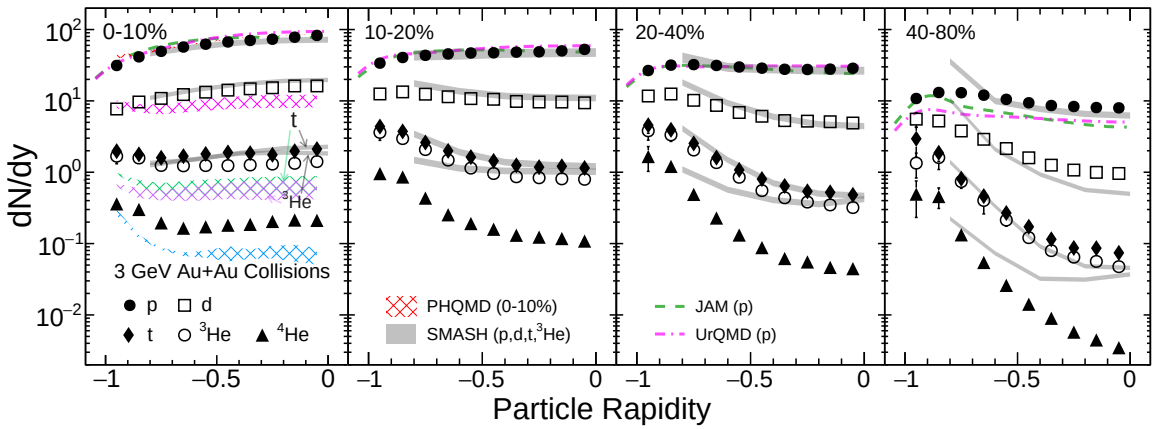

FIG. 8. Collision centrality dependence of primordial protons and light nuclei dN/dy from Au+Au collisions at $\sqrt{s_{\rm NN}} = 3\,{\rm GeV}$. The vertical lines represent the orthogonal sum of statistical and systematic errors. The gray bands and colored dotted lines are results from the hadronic transport model (SMASH of p, d, t, and ^{3}He, JAM and UrQMD of p) calculations for all centralities. The colored grid bands are results from PHQMD calculations of p, d, t, ^{3}He, and ^{4}He for the top 0-10% collisions.

TABLE V. Integral Yield (dN/dy) of inclusive and primordial protons at different centralities in Au+Au collisions at $\sqrt{s_{\rm NN}} =$ 3 GeV. The errors represent statistical and systematic uncertainties, respectively.

Rapidity	0-10%	10-20%	20-40%	40-80%
		Inclusive Proton		
-0.1 < y < 0	84.2269 ± 0.0065 ± 6.5297	53.5612 ± 0.0055 ± 3.8242	29.0693 ± 0.0030 ± 2.1287	7.8225 ± 0.0013 ± 0.7345
-0.2 < y < -0.1	79.7020 ± 0.0058 ± 5.2750	51.1497 ± 0.0048 ± 3.5403	28.2922 ± 0.0026 ± 2.0013	7.7403 ± 0.0011 ± 0.5458
-0.3 < y < -0.2	74.6585 ± 0.0052 ± 4.5472	49.6261 ± 0.0044 ± 2.9821	27.9482 ± 0.0024 ± 1.8241	8.0325 ± 0.0010 ± 0.4771
-0.4 < y < -0.3	71.6650 ± 0.0051 ± 4.8750	49.0187 ± 0.0044 ± 2.9275	28.1383 ± 0.0024 ± 1.9833	8.2011 ± 0.0011 ± 0.4955
-0.5 < y < -0.4	68.1892 ± 0.0050 ± 4.2165	47.9539 ± 0.0044 ± 3.0252	29.1134 ± 0.0025 ± 1.8381	8.9535 ± 0.0011 ± 0.7249
-0.6 < y < -0.5	63.3888 ± 0.0049 ± 3.8917	47.6113 ± 0.0044 ± 2.8138	30.2151 ± 0.0026 ± 2.1248	10.0751 ± 0.0012 ± 0.8930
-0.7 < y < -0.6	57.7172 ± 0.0048 ± 3.6508	46.1672 ± 0.0044 ± 2.6254	31.7023 ± 0.0027 ± 1.9231	11.5032 ± 0.0014 ± 0.8742
-0.8 < y < -0.7	50.1650 ± 0.0045 ± 3.0270	43.9809 ± 0.0045 ± 2.4251	32.5151 ± 0.0029 ± 2.0264	12.9956 ± 0.0015 ± 1.4232
-0.9 < y < -0.8	41.8546 ± 0.0043 ± 2.3117	40.9181 ± 0.0045 ± 2.3713	31.9247 ± 0.0030 ± 2.3222	13.6821 ± 0.0017 ± 1.6381
-1.0 < y < -0.9	31.7067 ± 0.0039 ± 1.9123	34.1028 ± 0.0043 ± 2.4771	26.8336 ± 0.0028 ± 1.6951	12.2254 ± 0.0017 ± 1.5859
		Primordial Proton		
-0.1 < y < 0	82.6797 ± 0.0069 ± 7.1551	52.6816 ± 0.0058 ± 4.5478	28.6342 ± 0.0031 ± 2.5641	7.7406 ± 0.0014 ± 0.7364
-0.2 < y < -0.1	78.1212 ± 0.0061 ± 5.8114	50.2430 ± 0.0050 ± 3.8371	27.8656 ± 0.0027 ± 2.3687	7.6617 ± 0.0012 ± 0.5569
-0.3 < y < -0.2	73.1433 ± 0.0054 ± 5.1103	48.7280 ± 0.0046 ± 3.2221	27.5364 ± 0.0025 ± 2.0731	7.9401 ± 0.0011 ± 0.5067
-0.4 < y < -0.3	70.3076 ± 0.0053 ± 5.5114	48.2161 ± 0.0046 ± 3.2354	27.7211 ± 0.0025 ± 2.1184	8.1217 ± 0.0011 ± 0.5011
-0.5 < y < -0.4	66.9528 ± 0.0052 ± 4.6377	47.1806 ± 0.0045 ± 3.3778	28.7408 ± 0.0026 ± 1.9352	8.8804 ± 0.0012 ± 0.7318
-0.6 < y < -0.5	62.3203 ± 0.0051 ± 4.2731	46.9185 ± 0.0046 ± 3.0108	29.8603 ± 0.0027 ± 2.1564	10.0022 ± 0.0013 ± 0.9445
-0.7 < y < -0.6	56.8581 ± 0.0049 ± 3.9454	45.5422 ± 0.0046 ± 2.7241	31.3767 ± 0.0028 ± 1.9461	11.4186 ± 0.0014 ± 1.0531
-0.8 < y < -0.7	49.5232 ± 0.0047 ± 3.2879	43.4985 ± 0.0046 ± 2.4453	32.2542 ± 0.0029 ± 2.2320	12.9221 ± 0.0016 ± 1.8662
-0.9 < y < -0.8	41.4016 ± 0.0044 ± 2.3341	40.5701 ± 0.0046 ± 2.4841	31.7371 ± 0.0030 ± 2.7653	13.6422 ± 0.0017 ± 2.1961
-1.0 < y < -0.9	31.3449 ± 0.0034 ± 2.0611	33.8040 ± 0.0039 ± 2.9454	26.6531 ± 0.0026 ± 1.8582	12.1841 ± 0.0015 ± 2.1424

total yield extraction, Table VII lists the percentage of dN/dy for the measured p_T range to the total dN/dy at all rapidity. The results for central and peripheral collisions provide a percentage range under different collision centralities. Calculations of proton and light nuclei dN/dy distributions using the hadronic transport models (JAM, PHQMD, SMASH, and UrQMD) were compared with the experimental data. The rapidity distributions of protons dN/dy in 0-10%, 10-20%, and 20-40% centrality bins can be well described by the models. For the SMASH model calculations of light nuclei (d, t, and ^{3}He), the Wigner function [38, 45, 46] was used to compute their formation probability. It was found that the rapidity distributions of d and t were well described by the SMASH model in central and mid-central collisions. On the other hand, in the PHQMD model calculations, clusters were dynamically formed using attractive interactions and identified with an advanced Minimum Spanning Tree (aMST) in coordinate space [44, 67]. The only parameter, the MST radius, is set to $r = 4\ fm$. As one can see in Fig. 8 (solid pink lines), in central collisions, although the PHQMD model result of proton rapidity distribution is consistent with data, the yields of d, t, ^{3}He, and ^{4}He were all underpredicted at mid-rapidity.

To obtain the yields for the full phase space (4π yields), the dN/dy distributions were fitted by the three-Gaussians function and the modified generalized Gaussian function [68–70], the latter can be expressed by Eq. 7.

TABLE VI. Integral Yield (dN/dy) of light nuclei at different centralities in Au+Au collisions at $\sqrt{s_{\rm NN}}$ = 3 GeV. The errors represent statistical and systematic uncertainties, respectively.

Rapidity	0-10%	10-20%	20-40%	40-80%
		Deuteron		
-0.1 < y < 0	16.2055 ± 0.0035 ± 2.2718	9.3904 ± 0.0029 ± 1.0265	4.8936 ± 0.0017 ± 0.3123	0.9668 ± 0.0008 ± 0.0586
-0.2 < y < -0.1	16.1856 ± 0.0030 ± 1.4321	9.6358 ± 0.0024 ± 1.1131	5.1030 ± 0.0014 ± 0.4626	0.9962 ± 0.0006 ± 0.0546
-0.3 < y < -0.2	15.2651 ± 0.0025 ± 1.1290	9.6575 ± 0.0021 ± 0.7286	5.1802 ± 0.0012 ± 0.3152	1.0728 ± 0.0005 ± 0.0989
-0.4 < y < -0.3	14.7571 ± 0.0025 ± 1.1883	9.8211 ± 0.0022 ± 0.7626	5.2948 ± 0.0012 ± 0.4964	1.2552 ± 0.0004 ± 0.0696
-0.5 < y < -0.4	14.1393 ± 0.0023 ± 1.0007	10.5301 ± 0.0020 ± 0.6487	6.0936 ± 0.0011 ± 0.4200	1.5903 ± 0.0005 ± 0.1167
-0.6 < y < -0.5	13.2526 ± 0.0022 ± 0.9648	10.8063 ± 0.0021 ± 0.8709	6.8961 ± 0.0012 ± 0.5749	2.1439 ± 0.0006 ± 0.1449
-0.7 < y < -0.6	12.2633 ± 0.0022 ± 0.7779	11.4487 ± 0.0022 ± 0.8635	8.6326 ± 0.0015 ± 0.4736	2.8985 ± 0.0007 ± 0.1725
-0.8 < y < -0.7	10.8655 ± 0.0021 ± 0.9661	12.4667 ± 0.0024 ± 0.9404	10.2733 ± 0.0016 ± 1.2942	3.8083 ± 0.0009 ± 0.2365
-0.9 < y < -0.8	9.6343 ± 0.0021 ± 0.6206	13.3361 ± 0.0026 ± 0.7320	12.5062 ± 0.0020 ± 1.0884	5.2252 ± 0.0011 ± 0.7009
-1.0 < y < -0.9	7.6776 ± 0.0020 ± 0.4384	12.3905 ± 0.0027 ± 1.0454	11.7238 ± 0.0020 ± 0.6558	5.5553 ± 0.0013 ± 1.2751
		Triton		
-0.1 < y < 0	2.0913 ± 0.0015 ± 0.2191	1.1445 ± 0.0013 ± 0.2144	0.4856 ± 0.0007 ± 0.0599	0.0746 ± 0.0003 ± 0.0151
-0.2 < y < -0.1	1.9739 ± 0.0012 ± 0.1842	1.2105 ± 0.0010 ± 0.1540	0.5220 ± 0.0005 ± 0.0558	0.0867 ± 0.0002 ± 0.0144
-0.3 < y < -0.2	1.7539 ± 0.0009 ± 0.1375	1.1792 ± 0.0008 ± 0.1381	0.5414 ± 0.0004 ± 0.0712	0.0867 ± 0.0002 ± 0.0066
-0.4 < y < -0.3	1.8515 ± 0.0008 ± 0.1254	1.2523 ± 0.0007 ± 0.0880	0.6438 ± 0.0004 ± 0.0439	0.1153 ± 0.0002 ± 0.0068
-0.5 < y < -0.4	1.8933 ± 0.0008 ± 0.1152	1.4409 ± 0.0008 ± 0.0875	0.8055 ± 0.0004 ± 0.0775	0.1721 ± 0.0002 ± 0.0159
-0.6 < y < -0.5	1.8016 ± 0.0007 ± 0.0992	1.6316 ± 0.0007 ± 0.0901	1.0800 ± 0.0004 ± 0.0686	0.2673 ± 0.0002 ± 0.0159
-0.7 < y < -0.6	1.6791 ± 0.0007 ± 0.0920	1.9951 ± 0.0008 ± 0.1103	1.6042 ± 0.0006 ± 0.0974	0.4626 ± 0.0003 ± 0.0280
-0.8 < y < -0.7	1.5980 ± 0.0007 ± 0.0888	2.6041 ± 0.0010 ± 0.1678	2.5242 ± 0.0007 ± 0.1573	0.8110 ± 0.0003 ± 0.0826
-0.9 < y < -0.8	1.7754 ± 0.0008 ± 0.1069	3.8254 ± 0.0013 ± 0.2850	3.9358 ± 0.0009 ± 0.2622	1.8718 ± 0.0006 ± 0.4538
-1.0 < y < -0.9	1.9749 ± 0.0009 ± 0.1246	4.3823 ± 0.0014 ± 0.5853	4.6199 ± 0.0010 ± 1.3601	2.9489 ± 0.0008 ± 1.3143
		^{3}He		
-0.1 < y < 0	1.4361 ± 0.0012 ± 0.1254	0.8050 ± 0.0011 ± 0.0717	0.3194 ± 0.0006 ± 0.0329	0.0476 ± 0.0003 ± 0.0066
-0.2 < y < -0.1	1.3468 ± 0.0009 ± 0.1217	0.8099 ± 0.0008 ± 0.0444	0.3481 ± 0.0004 ± 0.0431	0.0563 ± 0.0002 ± 0.0067
-0.3 < y < -0.2	1.3205 ± 0.0008 ± 0.0097	0.8434 ± 0.0007 ± 0.0643	0.3873 ± 0.0004 ± 0.0453	0.0648 ± 0.0001 ± 0.0083
-0.4 < y < -0.3	1.2696 ± 0.0008 ± 0.0078	0.8677 ± 0.0006 ± 0.0513	0.4395 ± 0.0003 ± 0.0372	0.0785 ± 0.0001 ± 0.0051
-0.5 < y < -0.4	1.2405 ± 0.0007 ± 0.0070	0.9597 ± 0.0006 ± 0.0662	0.5549 ± 0.0004 ± 0.0362	0.1203 ± 0.0002 ± 0.0095
-0.6 < y < -0.5	1.2434 ± 0.0007 ± 0.0074	1.1465 ± 0.0007 ± 0.0657	0.8450 ± 0.0005 ± 0.0468	0.2159 ± 0.0002 ± 0.0032
-0.7 < y < -0.6	1.2290 ± 0.0007 ± 0.0092	1.4973 ± 0.0009 ± 0.1317	1.3583 ± 0.0007 ± 0.0967	0.4154 ± 0.0003 ± 0.1300
-0.8 < y < -0.7	1.2451 ± 0.0008 ± 0.1163	2.0762 ± 0.0011 ± 0.1447	2.0529 ± 0.0009 ± 0.1236	0.7560 ± 0.0005 ± 0.1247
-0.9 < y < -0.8	1.5867 ± 0.0011 ± 0.1462	2.9643 ± 0.0015 ± 0.2644	3.1660 ± 0.0012 ± 0.4133	1.6094 ± 0.0009 ± 0.4884
-1.0 < y < -0.9	1.6674 ± 0.0012 ± 0.3469	4.0648 ± 0.0021 ± 1.2223	3.8249 ± 0.0015 ± 0.9857	1.3608 ± 0.0009 ± 0.4378
		^{4}He		
-0.1 < y < 0	0.2187 ± 0.0006 ± 0.0207	0.1023 ± 0.0005 ± 0.0179	0.0435 ± 0.0003 ± 0.0025	0.0033 ± 0.0001 ± 0.0002
-0.2 < y < -0.1	0.1943 ± 0.0005 ± 0.0162	0.1179 ± 0.0004 ± 0.0157	0.0447 ± 0.0002 ± 0.0037	0.0045 ± 0.0001 ± 0.0008
-0.3 < y < -0.2	0.1842 ± 0.0004 ± 0.0196	0.1229 ± 0.0003 ± 0.0114	0.0548 ± 0.0002 ± 0.0031	0.0058 ± 0.0001 ± 0.0003
-0.4 < y < -0.3	0.1778 ± 0.0003 ± 0.0102	0.1313 ± 0.0003 ± 0.0083	0.0620 ± 0.0001 ± 0.0054	0.0090 ± 0.0001 ± 0.0005
-0.5 < y < -0.4	0.1767 ± 0.0003 ± 0.0106	0.1582 ± 0.0003 ± 0.0087	0.0898 ± 0.0001 ± 0.0050	0.0142 ± 0.0001 ± 0.0008
-0.6 < y < -0.5	0.1693 ± 0.0002 ± 0.0103	0.1916 ± 0.0003 ± 0.0135	0.1335 ± 0.0002 ± 0.0073	0.0260 ± 0.0001 ± 0.0016
-0.7 < y < -0.6	0.1680 ± 0.0003 ± 0.0117	0.2530 ± 0.0003 ± 0.0189	0.2271 ± 0.0002 ± 0.0127	0.0548 ± 0.0001 ± 0.0030
-0.8 < y < -0.7	0.1993 ± 0.0003 ± 0.0131	0.4351 ± 0.0005 ± 0.0333	0.4917 ± 0.0004 ± 0.0287	0.1348 ± 0.0002 ± 0.0121
-0.9 < y < -0.8	0.3182 ± 0.0004 ± 0.0290	0.8622 ± 0.0007 ± 0.0929	1.2183 ± 0.0008 ± 0.2014	0.4572 ± 0.0004 ± 0.1385
-1.0 < y < -0.9	0.3631 ± 0.0006 ± 0.0280	0.9943 ± 0.0011 ± 0.2552	1.6292 ± 0.0014 ± 0.5169	0.5158 ± 0.0008 ± 0.2623

TABLE VII. The percentage (%) of the measured p_T range for primordial protons and light nuclei relative to the total dN/dy in 0-10% and 40-80% Au+Au collisions at $\sqrt{s_{\rm NN}}$ = 3 GeV. The errors are the combined statistical and systematic uncertainties.

Rapidity	Proton		Deuteron		Triton		^{3}He		^{4}He	
	0-10%	40-80%	0-10%	40-80%	0-10%	40-80%	0-10%	40-80%	0-10%	40-80%
-0.1 < y < 0	55 ± 4	39 ± 4	36 ± 5	14 ± 1	23 ± 2	6 ± 2	26 ± 2	7 ± 1	15 ± 1	4 ± 1
-0.2 < y < -0.1	66 ± 4	51 ± 4	50 ± 5	26 ± 1	38 ± 4	12 ± 2	42 ± 4	14 ± 2	25 ± 2	12 ± 2
-0.3 < y < -0.2	77 ± 5	63 ± 4	65 ± 5	42 ± 4	56 ± 4	25 ± 2	57 ± 4	27 ± 3	37 ± 4	21 ± 1
-0.4 < y < -0.3	77 ± 5	64 ± 4	64 ± 5	59 ± 3	74 ± 5	43 ± 3	74 ± 5	45 ± 3	66 ± 4	33 ± 2
-0.5 < y < -0.4	75 ± 5	61 ± 5	77 ± 6	57 ± 4	69 ± 4	39 ± 4	73 ± 4	41 ± 3	64 ± 4	51 ± 3
-0.6 < y < -0.5	73 ± 5	57 ± 5	75 ± 6	51 ± 3	84 ± 5	63 ± 4	68 ± 4	39 ± 6	77 ± 5	47 ± 3
-0.7 < y < -0.6	70 ± 4	52 ± 4	72 ± 5	47 ± 3	82 ± 5	60 ± 4	64 ± 5	37 ± 11	72 ± 5	42 ± 2
-0.8 < y < -0.7	67 ± 4	47 ± 5	68 ± 6	45 ± 3	79 ± 4	58 ± 6	55 ± 5	29 ± 5	66 ± 4	38 ± 3
-0.9 < y < -0.8	62 ± 3	42 ± 5	61 ± 4	37 ± 5	71 ± 4	44 ± 11	39 ± 4	16 ± 5	52 ± 5	26 ± 8
-1.0 < y < -0.9	57 ± 3	39 ± 5	54 ± 3	32 ± 7	63 ± 4	38 ± 17	32 ± 6	17 ± 5	24 ± 2	7 ± 4

$$Fitfunc. = p_0 \cdot \left(\frac{e^{-\frac{1}{2}\left(\frac{\log\left(1-\frac{k}{p}(x-x1)\right)}{k}\right)^2}}{\sqrt{2\pi}\cdot(p-k\cdot(x-x1))} + \frac{e^{-\frac{1}{2}\left(\frac{\log\left(1+\frac{k}{p}(x+x1)\right)}{k}\right)^2}}{\sqrt{2\pi}\cdot(p+k\cdot(x+x1))} \right) + p_4 \cdot e^{-\frac{1}{2}\cdot\left(\frac{x-p_5}{p_6}\right)^2} \quad (7)$$

where the parts in parentheses are the variant of the standard form of the generalized Gaussian function:

TABLE VIII. 4π yield for primordial protons and light nuclei. The errors represent statistical and systematic (from measurements and fitting, respectively) uncertainties.

Centrality	$0-10\%$	$10-20\%$	$20-40\%$	$40-80\%$
proton	$134.78 \pm 0.10 \pm 8.64 \pm 0.05$	$105.47 \pm 0.09 \pm 6.37 \pm 1.33$	$66.82 \pm 0.05 \pm 4.41 \pm 3.17$	$23.38 \pm 0.03 \pm 2.16 \pm 1.53$
deuteron	$29.03 \pm 0.05 \pm 2.09 \pm 0.17$	$27.34 \pm 0.05 \pm 1.77 \pm 1.84$	$19.33 \pm 0.03 \pm 1.20 \pm 3.29$	$6.66 \pm 0.01 \pm 0.45 \pm 1.28$
triton	$4.70 \pm 0.02 \pm 0.26 \pm 0.40$	$5.15 \pm 0.02 \pm 0.39 \pm 0.81$	$4.32 \pm 0.01 \pm 0.36 \pm 0.94$	$1.86 \pm 0.01 \pm 0.21 \pm 0.47$
^{3}He	$3.55 \pm 0.02 \pm 0.24 \pm 0.41$	$4.28 \pm 0.02 \pm 0.31 \pm 0.53$	$3.57 \pm 0.01 \pm 0.29 \pm 0.65$	$1.20 \pm 0.01 \pm 0.17 \pm 0.25$
^{4}He	$0.56 \pm 0.01 \pm 0.03 \pm 0.07$	$0.84 \pm 0.01 \pm 0.08 \pm 0.17$	$1.06 \pm 0.01 \pm 0.08 \pm 0.26$	$0.33 \pm 0.01 \pm 0.04 \pm 0.08$

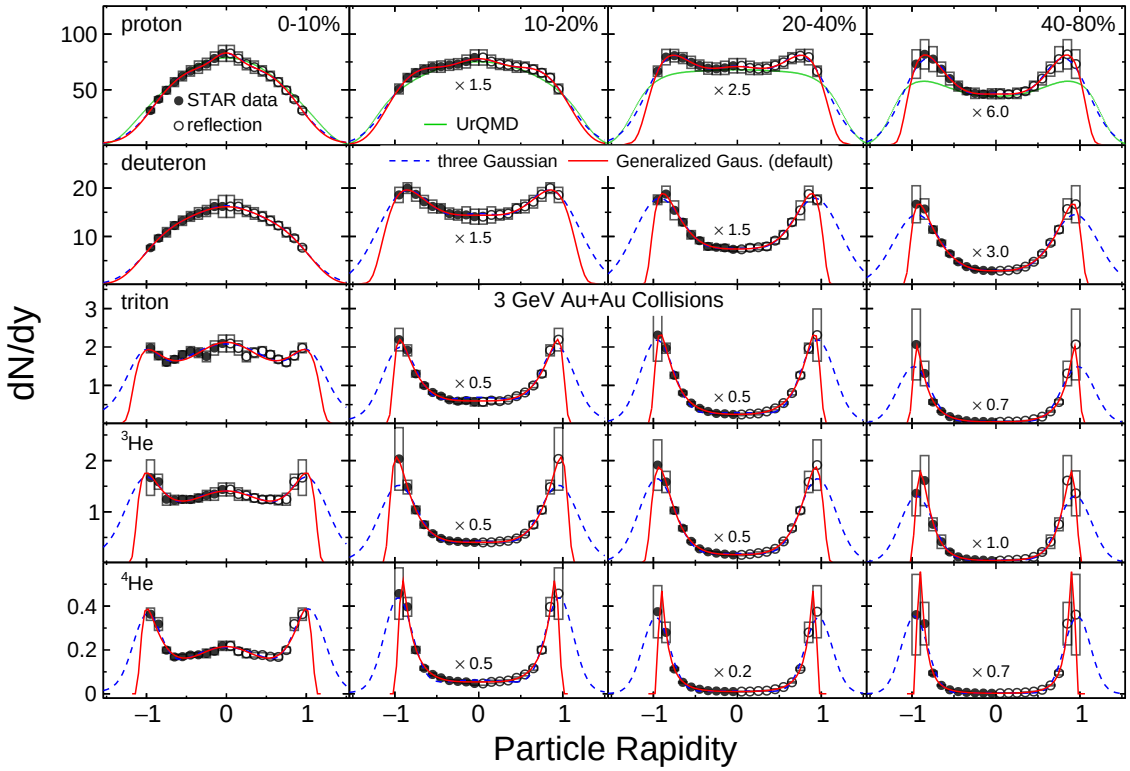

FIG. 9. Particle rapidity dependence of protons and light nuclei dN/dy from Au+Au collisions at $\sqrt{s_{\rm NN}} = 3\,{\rm GeV}$. For illustrative purposes, the maximum values of non-central collisions are scaled to the most central collision of the same particle. The blue and red lines represent the distribution fit by the three-Gaussians and the generalized Gaussian functions. The green line represents the proton distribution from the UrQMD model, with values scaled by the indicated factor between the model and the experiment at mid-rapidity.

$p(x;\alpha,\beta) = \frac{\alpha}{2\beta\Gamma(1/\alpha)} e^{-(|x|/\beta)^\alpha}, \alpha, \beta > 0$. The distribution is symmetric about $x = 0$ and has a sharp peak at $x = 0$. k, p, and $x1$ in the formula are given in the following forms:

$$A = p_3^2 + \sqrt{p_3^4 + 4p_3^2} + 2 \tag{8}$$

$$k = \sqrt{\log\left[\left(\frac{A}{2}\right)^{\frac{1}{3}} + \left(\frac{2}{A}\right)^{\frac{1}{3}} - 1\right]} \tag{9}$$

$$p = p_2 \cdot k \cdot \frac{e^{-\frac{1}{2}k^2}}{\sqrt{e^{k^2} - 1}} \tag{10}$$

$$x1 = \frac{p_1 \cdot k \cdot e^{k^2} + p\left(1 - e^{k^2}\right)}{k \cdot e^{k^2}} \tag{11}$$

with the above functions, the sharp peak will be at $x = \pm p_1$. p_2 is standard deviation, p_3 represents skewness. The part outside the parentheses is a Gaussian function with expectation value $p_5 = 0$.

The 4π yield was obtained by summing the true value of the measured region with the fitted value of the unmeasured region. As shown by the red and blue lines in Fig. 9, they represent the fitting results of the generalized Gaussian and three-Gaussians functions. The average of the two fits outside the target rapidity region ($1.0 < |y| < 2.0$) is used as the yield value of the extrapolation region.

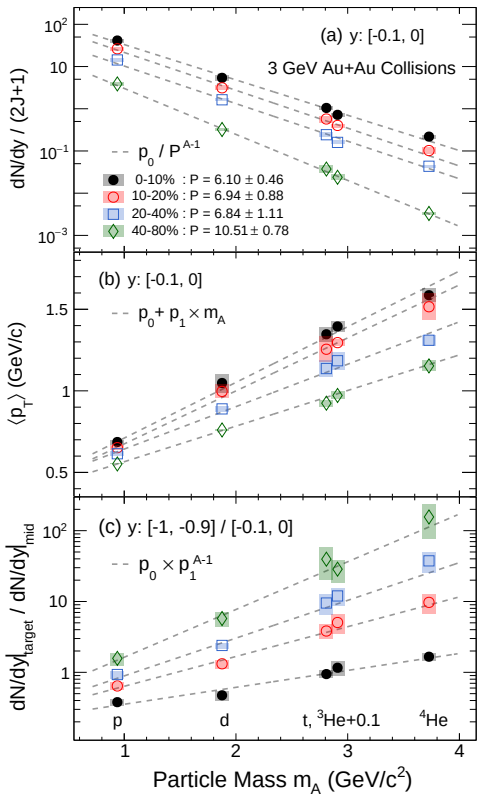

FIG. 10. (a) Mid-rapidity particle yields dN/dy, (b) mean transverse momentum $\langle p_T \rangle$, and (c) ratio of the dN/dy measured at target rapidity ($-1.0 < y < -0.9$) to mid-rapidity ($-0.1 < y < 0$) as a function of collision centrality and particle mass m_A (A is the mass number) from Au+Au collisions at $\sqrt{s_{\rm NN}} = 3$ GeV. For clarity, the mass of ^{3}He is shifted by 0.1 GeV/c^2. The boxes represent the quadratic sum of the measured statistical uncertainties and the extrapolation uncertainties. Dashed lines are fitting results of an exponential function to (a) the yields and (c) the yields ratio, and first-order polynomial (b) mean $\langle p_T \rangle$, respectively.

The systematic uncertainty of the 4π yield, in the measured rapidity region ($-1.0 < y < 0$), is the sum of the measured dN/dy systematic errors. For the unmeasured region, the discrepancy between the two fits described above was considered the systematic uncertainty. Finally, the systematic uncertainties of the 4π yields are 6-11% for protons, 7-20% for deuterons, 11-28% for tritons, 13-25% for ^{3}He, and 14-28% for ^{4}He. Table VIII lists the values, statistical, and systematic uncertainties for each particle and all centrality bins.

Figure 10 shows the mid-rapidity dN/dy, the dN/dy ratio of target rapidity ($-1.0 < y < -0.9$) to mid-rapidity ($-0.1 < y < 0$), and $\langle p_T \rangle$ as a function of particle mass for four centralities. The dN/dy values for different particles were scaled by their corresponding spin degeneracy factor $(2J + 1)$ [64, 71]. This scaling can be explained by the fact that the yield was found to be proportional to the spin coefficient in a statistical approach to light nuclei formation. This distribution was fit with an exponential function form: p_0/P^{A-1}, where P is the penalty factor and determined by the Boltzmann factor $e^{(m_N-\mu_B)/T}$ [20, 71–73]. The penalty factor is about 6.1 $\pm$ 0.5 and 10.5 $\pm$ 0.8 for the most central and peripheral Au+Au collisions at $\sqrt{s_{\rm NN}} = 3$ GeV, respectively. Figure 10 (b) shows that $\langle p_T \rangle$ increases linearly with increasing mass of the particle and exhibits centrality dependence. This indicates that the collective expansion in the radial direction is stronger in central collisions than in peripheral collisions. Figure 10 (c) shows the ratio of the dN/dy values measured at target rapidity to mid-rapidity as a function of particle mass. The ratio reveals the relative contributions of nuclear fragmentation to the yields of light nuclei at different collision centralities and particle mass. The ratio increases exponentially with increasing particle mass, with this upward trend being more pronounced in peripheral collisions compared to central collisions. It indicates that, from light to heavy nuclei, the proportion of contributions originating from the nuclear fragments increases.

D. Particle Ratio

Figure 11 shows the rapidity and centrality dependence of the light nuclei to proton yield ratios (d/p, t/p, ^{3}He/p, and ^{4}He/p) in Au+Au collisions at $\sqrt{s_{\rm NN}} = 3$ GeV. Based on the conclusions from the previous analysis of spectator contributions, it is found that these particle ratios monotonically decrease from target to mid-rapidity and show stronger rapidity dependence in peripheral collisions than in central collisions. The particle ratios calculated from the SMASH model are shown for comparison and denoted by the gray bands. In addition, using the parameters $T = 85$ MeV, $\mu_B = 728$ MeV [74], we estimated the mid-rapidity particle yield ratios in 0-10% central collisions from the thermal model without excited nuclei contributions [37, 74]. Figure 12 shows the energy dependence of the mid-rapidity ($-0.1 < y < 0$) d/p and t/p yield ratios in central Au+Au collisions. Both the d/p and t/p ratios at 3 GeV follow the world trend of energy dependence observed by the STAR Beam Energy Scan I [23, 24], FOPI [16, 35], and AGS [13, 14] experiments. The thermal model successfully predicts energy-dependent trends in d/p and t/p, but overestimates the values of d/p and t/p at 3 GeV.

E. Coalescence Parameter

In the coalescence model [75, 76], light nuclei are formed via the coalescence of their constituents (protons and neutrons), thus the relation between the momentum

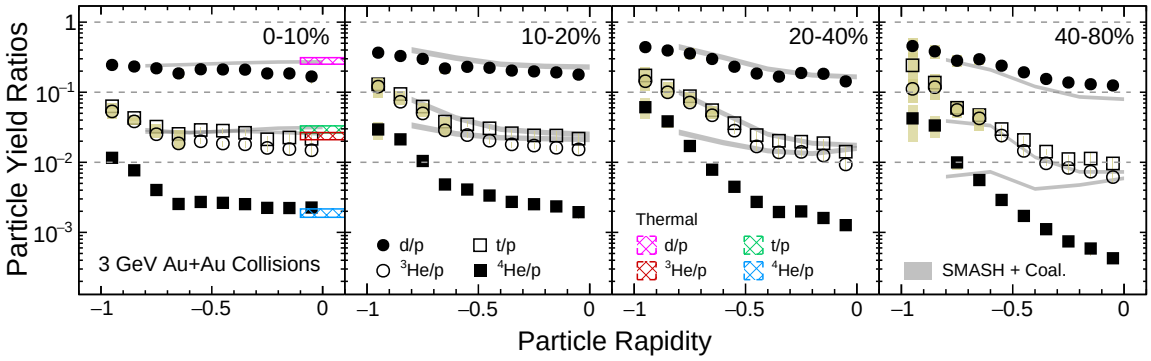

FIG. 11. Rapidity dependence of particle ratios d/p, t/p, ^{3}He/p, and ^{4}He/p for 0-10%, 10-20%, 20-40%, and 40-80% centralities in Au+Au collisions at $\sqrt{s_{\rm NN}} = 3\,$GeV. The vertical yellow areas represent the systematic uncertainties. Results of SMASH + Coalescence and thermal model calculations are shown as solid-gray bands and hatched-colored bands (mid-rapidity only), respectively.

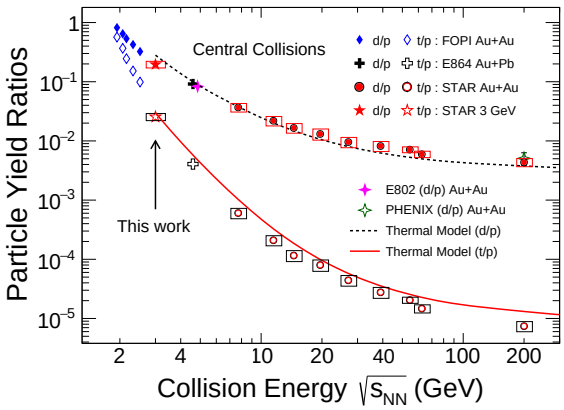

FIG. 12. Energy dependence of d/p (filled circle) and t/p (open circle) yield ratios. Statistical and systematic uncertainties are shown as vertical lines and boxes, respectively. The experimental results come from the STAR (0-10%), FOPI (impact parameter $b_0 < 0.15$), E864 (0-10%) and E802 (0-12%). The results from the thermal model are displayed as lines.

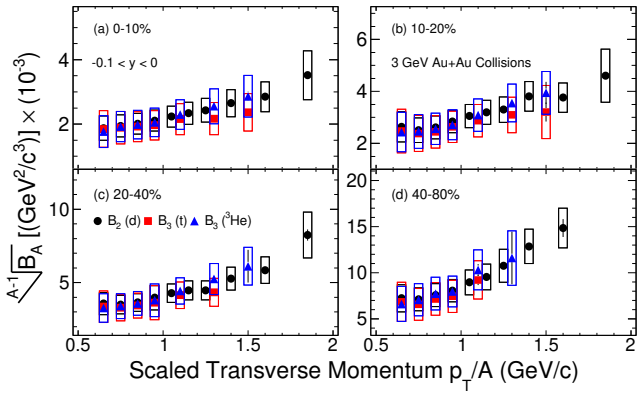

FIG. 13. Coalescence parameters $B_2(d)$, $\sqrt{B_3}(t)$, and $\sqrt{B_3}(^3\mathrm{He})$ as a function of p_T/A for different centrality bins in Au+Au collisions at $\sqrt{s_{\rm NN}} = 3\,$GeV. The boxes represent systematic uncertainties.

spectra of light nuclei, protons, and neutrons is as follows:

$$E_A\frac{d^3N_A}{d^3p_A} = B_A\left(E_p\frac{d^3N_p}{d^3p_p}\right)^Z\left(E_n\frac{d^3N_n}{d^3p_n}\right)^{A-Z} \approx (1.3)^{A-Z}B_A\left(E_p\frac{d^3N_p}{d^3p_p}\right)^A\Bigg|_{p_p=p_n=\frac{p_A}{A}} \quad (12)$$

where assume the same p_T, rapidity, and centrality dependence between protons and neutrons. The neutron spectrum is derived by scaling the proton spectrum with a factor of $n/p = 1.3 \pm 0.1$. This scaling factor is estimated from the $t/^3$He ratio [77] measured at 3 GeV, and this ratio is consistent with 1.28 calculated by the thermal model. $B_A \propto (1/V_{\rm eff})^{(A-1)}$ denotes the coalescence parameter, which is to reflect the coalescence probability of light nuclei with the mass number A. $V_{\rm eff}$ is the effective volume of the nucleon emission source.

Figure 13 describes the scaled transverse momentum dependence of the coalescence parameters for $B_2(d)$, $B_3(t)$, and $B_3(^3\mathrm{He})$ at mid-rapidity in 0-10%, 10-20%, 20-40%, and 40-80% centrality bins. Within the uncertainties, $^{A-1}\sqrt{B_A}$ of d, t, and ^{3}He are consistent, and their values increase with increasing p_T. This increasing trend can be explained by the presence of collective flow [78], and the length of homogeneity becomes smaller at higher transverse momentum [27]. Figure 14 shows the rapidity and centrality dependence of the coalescence parameters: B_2 for deuterons, $\sqrt{B_3}$ for tritons and ^{3}He at $p_T/A = 0.65\,$GeV/c. Both B_2 and $\sqrt{B_3}$ increase from central to peripheral collisions and, as mentioned before, these behaviors can be interpreted as the effective source volume getting smaller from central to peripheral collisions.

Figure 15 shows the energy dependence of the coalescence parameter in central heavy-ion collisions. The experimental data include the measurements from the EOS [20], NA44 [79], AGS [14, 80], PHENIX [81] and

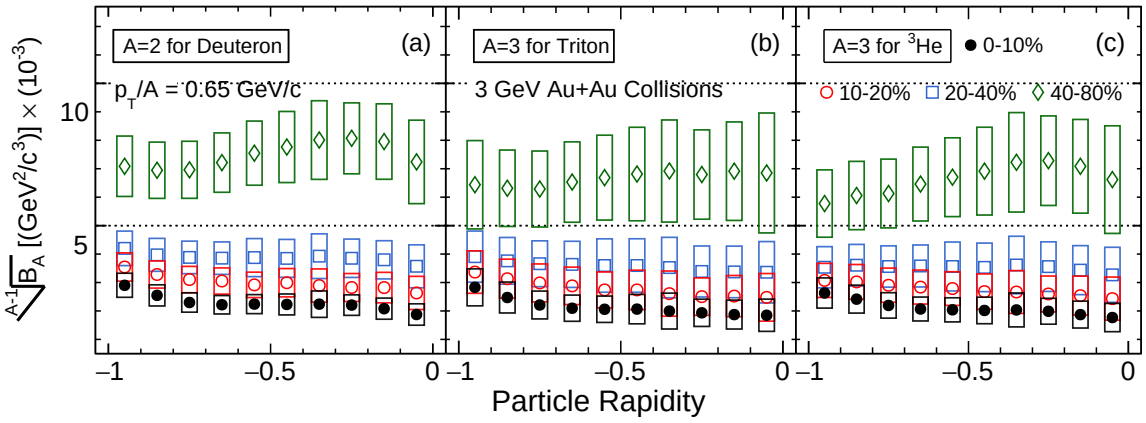

FIG. 14. Rapidity dependence of the coalescence parameter for $B_2(d)$, $B_3(t)$, and $B_3(^3\mathrm{He})$ at $p_T/A = 0.65\,\mathrm{GeV/c}$ for different centrality bins in Au+Au collisions at $\sqrt{s_{\mathrm{NN}}} = 3\,\mathrm{GeV}$. The boxes represent systematic uncertainties.

STAR BES-I [24, 82] experiments. The mid-rapidity $B_2(d)$, $B_3(t)$, and $B_3(^3\mathrm{He})$ with transverse momentum $p_T/A = 0.65\,\mathrm{GeV/c}$ at $\sqrt{s_{\mathrm{NN}}} = 3\,\mathrm{GeV}$ follows the world trend, and there is a clear upward trend towards low energy, which implies that the overall effective volume of the nucleon emitting source (V_{eff}) decreases with decreasing collision energies.

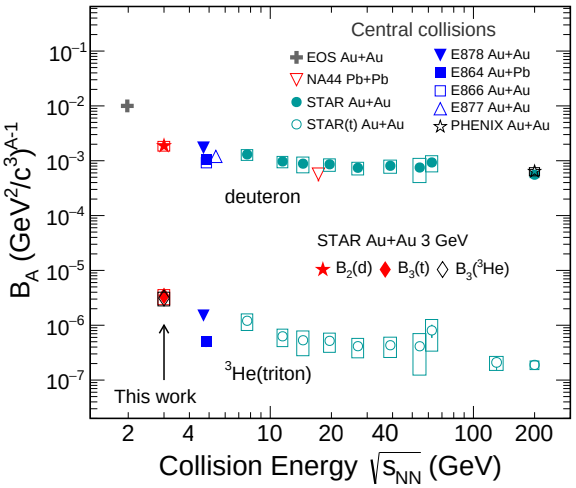

FIG. 15. Energy dependence of the coalescence parameters for $B_2(d)$, $B_3(t,^3\mathrm{He})$ in central collisions. The vertical lines indicate the statistical uncertainties. The boxes indicate systematic uncertainties. For comparison, the results from EOS [20], NA44 (0-10%) [79], AGS (0-10%) [14, 80], PHENIX (0-20%) [81] and STAR BES-I (0-10%) [24, 82] are also shown.

F. The Compound Yield Ratio of Light Nuclei

Based on the coalescence model [39], the compound yield ratio of tritons, deuterons, and protons ($N_t \times N_p/N_d^2$), was predicted to be sensitive to the neutron density fluctuations. Thus, it can be used to probe the signatures of the QCD critical point and/or the first-order phase transition in heavy-ion collisions. The STAR experiment has reported the centrality and the beam energy dependence of this yield ratio in Au+Au collisions at $\sqrt{s_{\mathrm{NN}}} = 7.7 - 200\,\mathrm{GeV}$ [24]. The yield ratio $N_p \times N_t/N_d^2$ monotonically decreases with increasing charged-particle multiplicity and shows scaling behavior regardless of the energy and centrality. This can be explained by the interplay between the finite size of light nuclei and system size in the coalescence model [27, 38, 83].

Figure 16 shows the centrality dependence of $N_t \times N_p/N_d^2$, $N_{^4\mathrm{He}} \times N_p/N_{^3\mathrm{He}} \times N_d$, and $N_{^4\mathrm{He}} \times N_d/(N_{^3\mathrm{He}} \times N_t)$. In each panel, the black solid and open circles denote the results from mid-rapidity and target rapidity, respectively. The experimental results presented in panels (a), (b), and (c) give almost no centrality dependence. Calculations from various models were applied to compare with the data. In panel (a), the results from the SMASH and UrQMD models [84] show monotonically increasing trends from central to peripheral collisions. The result from the thermal model calculation, which includes the decay from the excited nuclei to light nuclei (red band), is consistent with the experimental result in central collisions. In recent AMPT calculations [84], implementing a first-order phase transition gives a consistent description of the centrality dependence. Panel (b) depicts that the $N_{^4\mathrm{He}} \times N_p/(N_{^3\mathrm{He}} \times N_d)$ shows no centrality dependence, and the AMPT model also reproduces this centrality behavior. In the most central collisions, the results of the thermal model are lower than the experimental data whether or not the contribution of excited state decay was considered. In addition, the above two ratios are consistent with the calculations from PHQMD model within the larger uncertainty. In contrast to panel (b), the $N_{^4\mathrm{He}} \times N_d/(N_{^3\mathrm{He}} \times N_t)$ displayed in panel (c) demonstrate that the value from the thermal model is lower than the experimental result in central collisions, while from the PHQMD model is much higher, and that

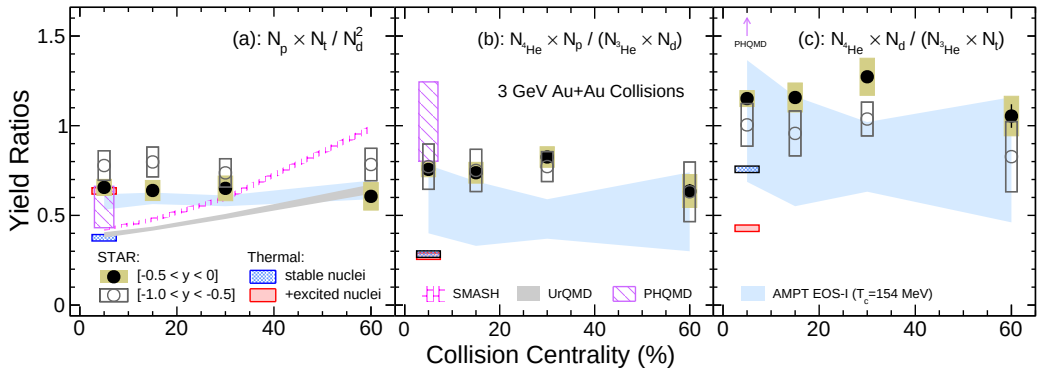

FIG. 16. Centrality and rapidity dependence of the yield ratios $N_p \times N_t/N_d^2$, $N_{^4\mathrm{He}} \times N_p/(N_{^3\mathrm{He}} \times N_d)$, and $N_{^4\mathrm{He}} \times N_d/(N_{^3\mathrm{He}} \times N_t)$ in Au+Au collisions at $\sqrt{s_{\mathrm{NN}}} = 3\,\mathrm{GeV}$. Solid and open markers indicate ratios from mid-rapidity ($-0.5 < y < 0$) and target rapidity ($-1 < y < -0.5$), respectively. Statistical uncertainties are smaller than the size of the markers and systematic uncertainties are shown by boxes. Results from hadronic transport models UrQMD, SMASH, and AMPT EoS-I are shown by colored bands. For the top 0-10% central collision, results from thermal and PHQMD models are also shown.

only the AMPT model can describe this centrality dependence.

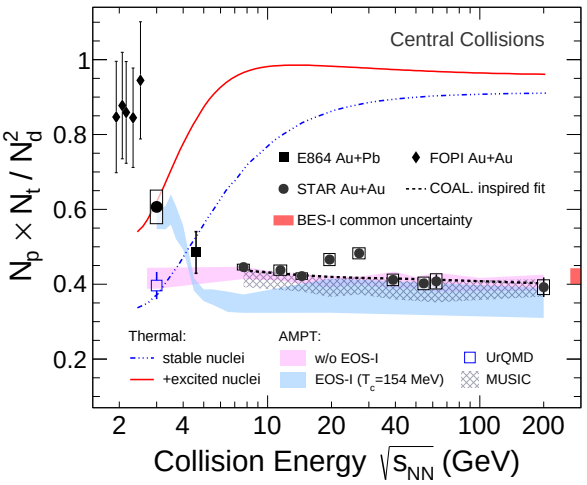

FIG. 17. Energy dependence of the ratio $N_p \times N_t/N_d^2$ in most central 0-10% Au + Au collisions. Vertical lines and boxes represent statistical and systematic uncertainties. The experimental results come from the STAR (0-10%), E864 (0-10%), and FOPI (impact parameter $b_0 < 0.15$). The red band at the right side of the plot indicates the common uncertainty (∼4.2%) in the BES-I result. Colored bands denote the ratios from MUSIC and AMPT (w/o and w/ EOS-I) hybrid model calculations. The ratio from UrQMD model is shown by an open square. Dashed black lines are the coalescence baselines obtained from the coalescence-inspired fit [85]. Solid red and dotted blue lines represent thermal model results.

The energy dependence of $N_t \times N_p/N_d^2$ in central heavy-ion collisions at mid-rapidity ($-0.5 < y < 0$) was presented in Fig. 17. The colored-bands and blue grid represent the calculations obtained from the hadronic transport model AMPT [84] and the hybrid model MUSIC+UrQMD [38], respectively. The black dashed line corresponds to the coalescence baseline obtained by fitting the charged-particle multiplicity dependence of the yield ratio from STAR BES-I data [24]. As mentioned earlier, this yield ratio is proposed as a sensitive observable to probe the nucleon density fluctaution near the QCD critical point and/or first order phase transition. The STAR experiment observed enhancements of the yield ratio relative to the coalescence baseline in 0-10% central Au+Au collisions at $\sqrt{s_{\mathrm{NN}}} = 19.6$ and 27 GeV [24], with a significance of 2.3σ and 3.4σ, respectively. At lower energies, the experimental results from the E864 [14], STAR and FOPI [16] experiments align with the world trend of the energy dependence and monotonically increase with decreasing energies. The thermal model, whether considering contributions from excited nuclear state decays or not, shows a monotonically increasing trend with increasing collision energies, eventually reaching a saturation at energies around a few tens of GeV. It was observed that the yield ratio at $\sqrt{s_{\mathrm{NN}}} = 3\,\mathrm{GeV}$ can be well described by the thermal model when incorporating the decays of excited nuclear states. Coalescence-based calculations of central Au+Au collisions at $\sqrt{s_{\mathrm{NN}}} = 3\,\mathrm{GeV}$ from UrQMD and AMPT models without considering the excited nuclear states decays show smaller values than the 3 GeV data. Furthermore, this yield ratio can be also reproduced by the AMPT model when employing a first-order phase transition. Those detailed comparisons between experimental data and various models calculations demonstrate that the production of light nuclei at mid-rapidity in Au+Au collisions at RHIC energies ($\sqrt{s_{\mathrm{NN}}} = 7.7$ - $200\,\mathrm{GeV}$) can be effectively explained by nucleon coalescence models. Additionally, it has been observed that the thermal model fails to describe the overall trend of the energy dependence of the yield ratios and the yields of light nuclei receive significant contributions from the decays of

excited nuclear states at lower energies.

IV. SUMMARY

We report the comprehensive measurement of protons (p) and light nuclei (d, t, ^{3}He, and ^{4}He) production from mid-rapidity to target rapidity in Au+Au collisions at $\sqrt{s_{\rm NN}} = 3\,{\rm GeV}$ by the STAR experiment. The p_T spectra, dN/dy, $\langle p_T \rangle$, particle yield ratios (d/p, t/p,^{3}He$/p$, ^{4}He$/p$), and coalescence parameters (B_2, B_3) are presented as a function of rapidity and collision centrality. The 4π yields are extracted based on the measured rapidity distributions of dN/dy. It is observed that the mid-rapidity dN/dy of protons and light nuclei can be well described by the exponential dependence of the particle mass via the Boltzmann factor $e^{(m_N-\mu_B)/T}$ [71, 86, 87]. The contributions from spectator fragmentations become more pronounced in peripheral collisions. The compound yield ratio $N_p \times N_t/N_d^2$ shows no centrality dependence for both mid-rapidity and target rapidity. Calculations of $N_p \times N_t/N_d^2$ from coalescence-based UrQMD and SMASH transport models show significant increasing trends from central to peripheral collisions, which fail to describe the experimental data [38, 85]. Furthermore, the increasing trend of the yield ratio $N_p \times N_t/N_d^2$ at energies below 4 GeV, which cannot be explained by thermal model or transport model calculations, suggests the presence of additional physics beyond the scope of these models. A recent AMPT calculation [84] incorporating a first-order phase transition can reproduce this increasing trend at low energies. The systematic measurements of the production of protons and light nuclei at 3 GeV provide valuable insights into the production dynamics of light nuclei and our understanding of the QCD phase structure at high baryon denisty.

V. ACKNOWLEDGEMENTS

We thank Drs. J. Aichelin, E. Bratkovskaya, C. Ko, J. Steinheimer, K. Sun, and W. Zhao for fruitful discussions about the production mechanism of light nuclei. We thank the RHIC Operations Group and RCF at BNL, the NERSC Center at LBNL, and the Open Science Grid consortium for providing resources and support. This work was supported in part by the Office of Nuclear Physics within the U.S. DOE Office of Science, the U.S. National Science Foundation, National Natural Science Foundation of China, Chinese Academy of Science, the Ministry of Science and Technology of China and the Chinese Ministry of Education, the Higher Education Sprout Project by Ministry of Education at NCKU, the National Research Foundation of Korea, Czech Science Foundation and Ministry of Education, Youth and Sports of the Czech Republic, Hungarian National Research, Development and Innovation Office, New National Excellency Programme of the Hungarian Ministry of Human Capacities, Department of Atomic Energy and Department of Science and Technology of the Government of India, the National Science Centre and WUT ID-UB of Poland, the Ministry of Science, Education and Sports of the Republic of Croatia, German Bundesministerium für Bildung, Wissenschaft, Forschung and Technologie (BMBF), Helmholtz Association, Ministry of Education, Culture, Sports, Science, and Technology (MEXT) and Japan Society for the Promotion of Science (JSPS).

[1] I. Arsene et al. (BRAHMS Collaboration), Nucl. Phys. A **757**, 1 (2005), nucl-ex/0410020.
[2] B. B. Back et al. (PHOBOS Collaboration), Nucl. Phys. A **757**, 28 (2005), nucl-ex/0410022.
[3] J. Adams et al. (STAR Collaboration), Nucl. Phys. A **757**, 102 (2005), nucl-ex/0501009.
[4] J. Chen, D. Keane, Y.-G. Ma, A. Tang, and Z. Xu, Phys. Rept. **760**, 1 (2018), 1808.09619.
[5] X. Luo, Q. Wang, N. Xu, and P. Zhuang, eds., *Properties of QCD Matter at High Baryon Density* (Springer, 2022), ISBN 978-981-19444-0-6, 978-981-19444-1-3.
[6] Y. Aoki, G. Endrodi, Z. Fodor, S. D. Katz, and K. K. Szabo, Nature **443**, 675 (2006), hep-lat/0611014.
[7] M. A. Stephanov, K. Rajagopal, and E. V. Shuryak, Phys. Rev. D **60**, 114028 (1999), hep-ph/9903292.
[8] S. Ejiri, Phys. Rev. D **78**, 074507 (2008), 0804.3227.
[9] B. Borderie and J. D. Frankland, Prog. Part. Nucl. Phys. **105**, 82 (2019), 1903.02881.
[10] M. M. Aggarwal et al. (STAR Collaboration) (2010), 1007.2613.
[11] X. Luo and N. Xu, Nucl. Sci. Tech. **28**, 112 (2017), 1701.02105.
[12] J. Barrette et al. (E814 Collaboration), Phys. Rev. C **50**, 1077 (1994).
[13] L. Ahle et al. (E802 Collaboration), Phys. Rev. C **60**, 064901 (1999).
[14] T. A. Armstrong et al. (E864 Collaboration), Phys. Rev. C **61**, 064908 (2000), nucl-ex/0003009.
[15] S. Albergo et al., Phys. Rev. C **65**, 034907 (2002).
[16] W. Reisdorf et al. (FOPI Collaboration), Nucl. Phys. A **848**, 366 (2010), 1005.3418.
[17] B. I. Abelev et al. (STAR), Science **328**, 58 (2010), 1003.2030.
[18] H. Agakishiev et al. (STAR Collaboration), Nature **473**, 353 (2011), [Erratum: Nature 475, 412 (2011)], 1103.3312.
[19] J. Adam et al. (ALICE Collaboration), Phys. Rev. C **93**, 024917 (2016), 1506.08951.
[20] T. Anticic et al. (NA49 Collaboration), Phys. Rev. C **94**, 044906 (2016), 1606.04234.
[21] L. Adamczyk et al. (STAR Collaboration), Phys. Rev. C **94**, 034908 (2016), 1601.07052.
[22] S. Acharya et al. (ALICE Collaboration), Phys. Rev. C **97**, 024615 (2018), 1709.08522.

[23] J. Adam et al. (STAR Collaboration), Phys. Rev. C **99**, 064905 (2019), 1903.11778.
[24] M. I. Abdulhamid et al. (STAR Collaboration), Phys. Rev. Lett. **130**, 202301 (2023).
[25] H. Sato and K. Yazaki, Phys. Lett. B **98**, 153 (1981).
[26] C. B. Dover, U. W. Heinz, E. Schnedermann, and J. Zimanyi, Phys. Rev. C **44**, 1636 (1991).
[27] R. Scheibl and U. W. Heinz, Phys. Rev. C **59**, 1585 (1999), nucl-th/9809092.
[28] Y. Oh, Z.-W. Lin, and C. M. Ko, Phys. Rev. C **80**, 064902 (2009), 0910.1977.
[29] A. Andronic, P. Braun-Munzinger, J. Stachel, and H. Stocker, Phys. Lett. B **697**, 203 (2011), 1010.2995.
[30] J. Cleymans, S. Kabana, I. Kraus, H. Oeschler, K. Redlich, and N. Sharma, Phys. Rev. C **84**, 054916 (2011), 1105.3719.
[31] N. Shah, Y. G. Ma, J. H. Chen, and S. Zhang, Phys. Lett. B **754**, 6 (2016), 1511.08266.
[32] K.-J. Sun, L.-W. Chen, C. M. Ko, and Z. Xu, Phys. Lett. B **774**, 103 (2017), 1702.07620.
[33] A. Andronic, P. Braun-Munzinger, K. Redlich, and J. Stachel, Nature **561**, 321 (2018), 1710.09425.
[34] P. Braun-Munzinger and B. Dönigus, Nucl. Phys. A **987**, 144 (2019), 1809.04681.
[35] E. Shuryak and J. M. Torres-Rincon, Eur. Phys. J. A **56**, 241 (2020), 2005.14216.
[36] B. Dönigus, Int. J. Mod. Phys. E **29**, 2040001 (2020), 2004.10544.
[37] V. Vovchenko, B. Dönigus, B. Kardan, M. Lorenz, and H. Stoecker, Phys. Lett. **B**, 135746 (2020), 2004.04411.
[38] W. Zhao, K.-j. Sun, C. M. Ko, and X. Luo, Phys. Lett. B **820**, 136571 (2021), 2105.14204.
[39] K.-J. Sun, L.-W. Chen, C. M. Ko, J. Pu, and Z. Xu, Phys. Lett. B **781**, 499 (2018), 1801.09382.
[40] E. Shuryak and J. M. Torres-Rincon, Phys. Rev. C **101**, 034914 (2020), 1910.08119.
[41] Y. Nara, EPJ Web Conf. **208**, 11004 (2019).
[42] J. Weil et al. (SMASH Collaboration), Phys. Rev. C **94**, 054905 (2016), 1606.06642.
[43] S. A. Bass et al., Prog. Part. Nucl. Phys. **41**, 255 (1998), nucl-th/9803035.
[44] S. Gläßel, V. Kireyeu, V. Voronyuk, J. Aichelin, C. Blume, E. Bratkovskaya, G. Coci, V. Kolesnikov, and M. Winn, Phys. Rev. C **105**, 014908 (2022), 2106.14839.
[45] L.-W. Chen, C. M. Ko, and B.-A. Li, Phys. Rev. C **68**, 017601 (2003), nucl-th/0302068.
[46] W. Zhao, L. Zhu, H. Zheng, C. M. Ko, and H. Song, Phys. Rev. C **98**, 054905 (2018), 1807.02813.
[47] J. Adam et al. (STAR Collaboration), Phys. Rev. C **103**, 034908 (2021), 2007.14005.
[48] M. S. Abdallah et al. (STAR Collaboration), Phys. Rev. Lett. **128**, 202303 (2022), 2112.00240.
[49] Y. J. Sun et al., Nucl. Instrum. Meth. A **593**, 307 (2008), 0805.2459.
[50] F. S. Bieser et al., Nucl. Instrum. Meth. A **499**, 766 (2003).
[51] W. J. Llope (STAR Collaboration), Nucl. Instrum. Meth. A **661**, S110 (2012).
[52] M. Anderson et al., Nucl. Instrum. Meth. A **499**, 659 (2003), nucl-ex/0301015.
[53] M. Shao, O. Y. Barannikova, X. Dong, Y. Fisyak, L. Ruan, P. Sorensen, and Z. Xu, Nucl. Instrum. Meth. A **558**, 419 (2006), nucl-ex/0505026.
[54] M. Abdallah et al. (STAR), Phys. Rev. C **104**, 024902 (2021), 2101.12413.
[55] J. PFANZAGL and O. SHEYNIN, Biometrika **83**, 891 (1996), ISSN 0006-3444, https://academic.oup.com/biomet/article-pdf/83/4/891/703592/83-4-891.pdf, URL https://doi.org/10.1093/biomet/83.4.891.
[56] C. Adler et al. (STAR Collaboration), Phys. Rev. Lett. **87**, 262302 (2001), nucl-ex/0110009.
[57] J. Adam et al. (STAR), Phys. Rev. C **102**, 034909 (2020), 1906.03732.
[58] K. Adcox et al. (PHENIX Collaboration), Phys. Rev. Lett. **89**, 092302 (2002), nucl-ex/0204007.
[59] T. Anticic et al. (NA49 Collaboration), Phys. Rev. C **83**, 014901 (2011), 1009.1747.
[60] D. Oliinychenko, C. Shen, and V. Koch (SMASH Collaboration), Phys. Rev. C **103**, 034913 (2021), 2009.01915.
[61] M. S. Abdallah et al. (STAR Collaboration), Phys. Lett. B **831**, 137152 (2022), 2108.00924.
[62] M. Tanabashi et al. (Particle Data Group), Phys. Rev. D **98**, 030001 (2018).
[63] G.-C. Yong, B.-A. Li, Z.-G. Xiao, and Z.-W. Lin, Phys. Rev. C **106**, 024902 (2022), 2206.10766.
[64] A. Andronic, P. Braun-Munzinger, and J. Stachel, Nucl. Phys. A **772**, 167 (2006), nucl-th/0511071.
[65] E. Schnedermann, J. Sollfrank, and U. W. Heinz, Phys. Rev. C **48**, 2462 (1993), nucl-th/9307020.
[66] J. P. Bondorf, A. S. Botvina, A. S. Ilinov, I. N. Mishustin, and K. Sneppen, Phys. Rept. **257**, 133 (1995).
[67] E. Bratkovskaya, S. Glässel, V. Kireyeu, J. Aichelin, M. Bleicher, C. Blume, G. Coci, V. Kolesnikov, J. Steinheimer, and V. Voronyuk, EPJ Web Conf. **276**, 03005 (2023), 2208.11802.
[68] P. Moulin and J. Liu, IEEE Transactions on Information Theory **45**, 909 (1999).
[69] G. Verdoolaege and P. Scheunders, International Journal of Computer Vision **95**, 265 (2011), URL https://doi.org/10.1007/s11263-011-0448-9.
[70] G. Verdoolaege and P. Scheunders, Journal of Mathematical Imaging and Vision **43**, 180 (2012), URL https://doi.org/10.1007/s10851-011-0297-8.
[71] T. A. Armstrong et al. (E864 Collaboration), Phys. Rev. Lett. **83**, 5431 (1999), nucl-ex/9907002.
[72] P. Braun-Munzinger and J. Stachel, J. Phys. G **21**, L17 (1995), nucl-th/9412035.
[73] J. Steinheimer, Z. Xu, K. Gudima, A. Botvina, I. Mishustin, M. Bleicher, and H. Stocker, J. Phys. Conf. Ser. **389**, 012022 (2012).
[74] V. Vovchenko, V. V. Begun, and M. I. Gorenstein, Phys. Rev. C **93**, 064906 (2016), 1512.08025.
[75] S. T. Butler and C. A. Pearson, Phys. Rev. **129**, 836 (1963).
[76] N. Yu, D. Zhang, and X. Luo, Chin. Phys. C **44**, 014002 (2020), 1812.04291.
[77] V. I. Kolesnikov (NA49), J. Phys. Conf. Ser. **110**, 032010 (2008), 0710.5118.
[78] A. Polleri, J. P. Bondorf, and I. N. Mishustin, Phys. Lett. B **419**, 19 (1998), nucl-th/9711011.
[79] I. G. Bearden et al., Eur. Phys. J. C **23**, 237 (2002).
[80] M. J. Bennett et al. (E878 Collaboration), Phys. Rev. C **58**, 1155 (1998).
[81] S. S. Adler et al. (PHENIX Collaboration), Phys. Rev. Lett. **94**, 122302 (2005), nucl-ex/0406004.

[82] C. Adler et al. (STAR Collaboration), Phys. Rev. Lett. **87**, 262301 (2001), [Erratum: Phys.Rev.Lett. 87, 279902 (2001)], nucl-ex/0108022.
[83] L. P. Csernai and J. I. Kapusta, Phys. Rept. **131**, 223 (1986).
[84] K.-J. Sun, W.-H. Zhou, L.-W. Chen, C. M. Ko, F. Li, R. Wang, and J. Xu (2022), 2205.11010.
[85] K.-J. Sun, C. M. Ko, and B. Dönigus, Phys. Lett. B **792**, 132 (2019), 1812.05175.
[86] J. L. Nagle, B. S. Kumar, D. Kusnezov, H. Sorge, and R. Mattiello, Phys. Rev. C **53**, 367 (1996).
[87] S. Das Gupta and A. Z. Mekjian, Phys. Rept. **72**, 131 (1981).